SEDIMENTOLOGY the journal of the International Association of Sedimentologists IAS

Sedimentology (2024) doi: 10.1111/sed.13178

Autogenic evolution of valley-confined deltas during sea-level rise: Insights from numerical and physical modelling

RU WANG*,† , WONSUCK KIM* , LUCA COLOMBERA‡ , NIGEL P. MOUNTNEY† , YUNHYEONG LEE* and JAEHYUNG LEE*

**Department of Earth System Sciences, Yonsei University, Seoul 03722, Korea (E-mail: earrwa@leeds.ac.uk) (E-mail: delta@yonsei.ac.kr)*

†School of Earth and Environment, University of Leeds, Leeds LS2 9JT, UK

‡Department of Earth and Environmental Sciences, University of Pavia, Pavia, Italy

Associate Editor – Kyle Straub

ABSTRACT

Nearshore incised valleys are important conduits for the transport of sediment, nutrients, pollutants and organic carbon from the continents to the sea. Therefore, it is essential to understand the autogenic evolution of deltas confined within incised valleys and how such evolution is affected by relative sea-level rise. To date, limited research has focused on how deltas constrained by incised valleys or other forms of antecedent topography respond to rising sea level. An existing theory of autostratigraphy envisages scenarios in which two-dimensional or unconfined three-dimensional fan deltas can experience three evolutionary stages under constant rates of relative sea-level rise and sediment supply: progradation, autoretreat and post-autobreak transgression. In this work, an integrated study of geometric numerical models and physical experiments is undertaken to investigate autostratigraphic delta evolution for a variety of incised-valley geometries, under conditions of constant rates of relative sea-level rise and sediment supply. Results indicate that interplays of antecedent topography (valley geometries) and sediment mass balance expressed in resultant deltaic geometries can result in autogenic changes in shoreline dynamics and river avulsion frequency on deltas. The following primary findings arise. (i) Compared to valleys with rectangular and trapezoidal cross-sectional profiles, valleys with triangular cross-sections tend to contain deltas that experience faster rates of progradation, autoretreat and post-autobreak transgression under rising sea level, and exhibit a more prominent convex-seaward shoreline trajectory. (ii) The shoreline trajectory is also related to delta topset geometry, becoming more convex-seaward under decreasing topset slopes. (iii) River avulsion frequency on deltas with rising sea level varies markedly across valleys with different geometries, even under the same rate of relative sea-level rise; this is attributed to the difference in temporal evolution of shoreline migration for different valley geometries and the resultant difference in the delta topset aggradation. This study highlights complexities in responses of sedimentary systems under the confinement of different topographic configurations that have hitherto largely been overlooked in sequence-stratigraphic models. The findings provide insight into future shoreline behaviour and river avulsion hazard on confined deltas, and for decoding the stratigraphic record.

Keywords Autogenic process, avulsion, incised valley, sea-level change, shoreline migration.

INTRODUCTION

Nearshore incised valleys are fluvially eroded, elongate (palaeo) topographic lows carved into coastal plains and/or shelves. Typically, they develop as rivers erode their bed in response to one or more episodes of relative sea-level (RSL) fall, and are inundated and infilled during one or more ensuing episodes of RSL rise (Dalrymple & Zaitlin, 1994; Posamentier & Allen, 1999; Blum *et al.*, 2013). Nearshore incised valleys are conduits for the transfer of particulates from continents to the shelf break (Blum *et al.*, 2013) and therefore are globally important in regard to transport of sediment, nutrients, pollutants, and organic carbon from rivers and coasts to all marine environments. Characterization of the stratigraphic architecture of nearshore incised valleys and their infills provides insights into the relationship between external controls (for example, eustatic fluctuations) and stratigraphic architectures (e.g. Posamentier *et al.*, 1988; Posamentier & Vail, 1988; Van Wagoner *et al.*, 1990; Shanley & McCabe, 1994; Blum & Törnqvist, 2000; Catuneanu, 2006; Holbrook *et al.*, 2006). Many incised-valley fills (IVFs) have excellent potential as hydrocarbon reservoirs, groundwater aquifers and sites for the underground storage of CO_2 (e.g. Hampson *et al.*, 1999; Stephen & Dalrymple, 2002; Bowen & Weimer, 2003; Salem *et al.*, 2005). This is due to the common occurrence of IVFs comprising relatively coarse-grained fluvial lowstand strata that are overlain by relatively fine-grained estuarine mud-prone deposits, all potentially encased in mud-dominated coastal-plain or shelf deposits (Zaitlin *et al.*, 1994). Many modern flooded river valleys (estuaries and rias) and deltas developed atop filled incised valleys host large human populations. Examples include major estuaries along the United States coastline of the Gulf of Mexico, such as the Trinity, Sabine and Neches valleys; the Fly estuary in Papua New Guinea; the Changjiang estuary in China; the Mississippi delta in the US; and the Tiber delta in Italy.

Much prior work has focused on the characterization of the morphology of incised valleys and the stratigraphic organization of their infills (e.g. Dalrymple *et al.*, 1992; Zaitlin *et al.*, 1994; Blum *et al.*, 2013; Wang *et al.*, 2019, 2020). These studies emphasized the role of allogenic controls. Only a relatively small number of studies have instead been undertaken to investigate the role of autogenic processes on the stratigraphic architecture of IVFs, primarily with a focus on the effect of the antecedent topography of the underlying incised valley (e.g. Rodriguez *et al.*, 2005; Simms & Rodriguez, 2014, 2015; Sahoo & Gani, 2016; Guerit *et al.*, 2020).

In this study, the overall aim is to investigate the autogenic evolution of deltas confined within incised valleys during RSL rise. The following specific research questions are addressed: (i) How do shoreline migration patterns, quantified by shoreline trajectories and shoreline migration rates (Helland-Hansen & Martinsen, 1996), vary in response to RSL rise for valleys and in-valley deltas of variable geometries? (ii) How do delta-top aggradation rate and valley-confined fluvio-deltaic system avulsion frequency vary in response to RSL rise for different types of valley geometries? (iii) What is the link between surface morphodynamics and resultant subsurface fluvial stratigraphy when deltas are confined by incised valleys or other forms of antecedent topography?

To address these questions, the following two research activities are undertaken. (i) Development of a series of numerical geometric models with which to determine dynamic shoreline migration patterns, delta-top aggradation rates, and the characteristic avulsion timescales of the in-valley fluvio-deltaic system for different valley geometries under conditions of constant rates of RSL rise and sediment supply. (ii) Implementation of a series of physical experiments to test the applicability of the numerical predictions derived from the above-mentioned geometric models.

The results are discussed considering their implications for sequence-stratigraphic models and interpretations of the stratigraphic record, and for prediction of future shoreline behaviour and avulsion-related natural hazards. Note that the autogenic shoreline shifts and the channel dynamics examined here occur at different hierarchical levels: the former is a larger scale, deterministic mechanism whereas the latter is a smaller scale, partially stochastic mechanism (Hajek & Straub, 2017).

METHODOLOGY

In this work, complementary geometric-based numerical models and physical experiments are employed to investigate the effects of the geometries of valleys and in-valley deltas on shoreline migration patterns and associated channel dynamics. In the following sections, a summary of the methods used for the geometric

modelling and the physical experiments is presented. More detailed descriptions and explanations of the methods are provided in the Supporting Information.

Valley geometries

In nature, valley morphology varies markedly along both dip and strike orientations (Anderson *et al.*, 2004; Wang *et al.*, 2019, 2020). For instance, some valleys deepen seaward, whereas others become shallower; some valley margins exhibit a terraced morphology, whereas others are V-shaped or U-shaped in strike-oriented cross-section. Moreover, along continental margins, valley incision commonly commences where a convex-up topography is exposed during RSL fall (Summerfield, 1985; Talling, 1998; Blum & Törnqvist, 2000; Blum *et al.*, 2013). As such, the deepest and widest parts of incised valleys are expected to occur in correspondence with pre-existing convex-up topographies (e.g. Talling, 1998). This mostly occurs either at the position of the highstand shoreline or at the continental shelf-slope break. Hence, in the geometric-based numerical modelling and/or physical experiments presented here, valleys with the following geometries are considered: (i) valleys with morphologies that remain constant along the valley axis, and which exhibit rectangular (Fig. 1A), trapezoidal (Fig. 1B), triangular (Fig. 1C) or terraced strike cross-sectional shapes (Fig. 1D); (ii) a valley with a geometry that deepens and widens seaward (Fig. 1E); and (iii) a valley with a geometry that narrows and shallows both seaward and landward of the deepest and widest point located near the slope break (Fig. 1F). For simplicity, hereafter, valleys with a rectangular, triangular, trapezoidal or terraced strike cross-sectional profile and constant morphology in the dip direction are termed 'simple valley geometries'; the other two valley types with geometries that vary longitudinally are termed 'complex valley geometries'.

Geometric modelling

Shoreline migration patterns for simple valley geometries

For valleys with simple geometries (Fig. 1A to D), the shoreline migration patterns are simulated based on sediment mass balance, under prescribed 'three-dimensional' delta and valley geometries during constant rates of RSL rise and sediment supply (cf. Muto, 2001; Muto *et al.*, 2007). Accommodation is created through time due to RSL rise causing valley inundation and is dominantly consumed by deltaic sedimentation. Here, accommodation is defined as the volume that exists inside the valley between the sea level and the initial valley form (cf. Rodriguez *et al.*, 2008; Guerit *et al.*, 2020). Only the accommodation that exists in the subaqueous part of a flooded incised valley, which controls shoreline dynamics, is considered. Aggradation on interfluves, and more generally beyond the confines of the valley, is not modelled herein; this quantification of accommodation is suitable for the scopes of this study.

In this work, following the assumptions made by previous work on numerical modelling of IVFs (Simms & Rodriguez, 2014, 2015; Guerit *et al.*, 2020), the current model assumes that: (i) the delta is always confined by the valley sidewalls; (ii) the width of the delta equals the width of the flooded valley; (iii) sedimentation in the central basin (i.e. the central parts of valley-confined estuarine basins) is negligible; and (iv) the influence of waves and tides is also negligible during the modelling run. The current model considers a longitudinally uniform valley with a flat valley thalweg, a width W, a height H, a horizontal length L_v, and/or a valley sidewall slope θ, and a valley-confined delta with fixed-gradient topset S_t and foreset S_f (Fig. 1A to D).

Choices made in the modelling approach have been informed by previous work on the effect of RSL rise on the two-dimensional (width-averaged) evolution of alluvial deltas via physical modelling (e.g. Muto, 2001) and numerical modelling (e.g. Parker *et al.*, 2008a,b). These earlier studies demonstrated that, under conditions of constant rates of RSL rise and sediment supply, both the delta shoreline (topset–foreset break) and delta toe (foreset downlap) prograde seaward initially, though at progressively decreasing rates (Fig. 1G). Eventually, after a sufficiently long period of RSL rise, the delta topset–foreset break starts to retrograde landward, even though the delta toe continues to advance seaward. This mechanism is termed 'autoretreat' (Muto, 2001). Such retreat results from a progressive increase of the entire surface area of the delta with time (subaerial and subaqueous) and a resultant decrease of sediment flux across the delta topset–foreset break for a constant rate of sediment supply (Muto & Steel, 1992, 1997; Milton & Bertram, 1995). With continuing sea-level rise, sediment delivery to the delta topset–foreset break will gradually decrease to

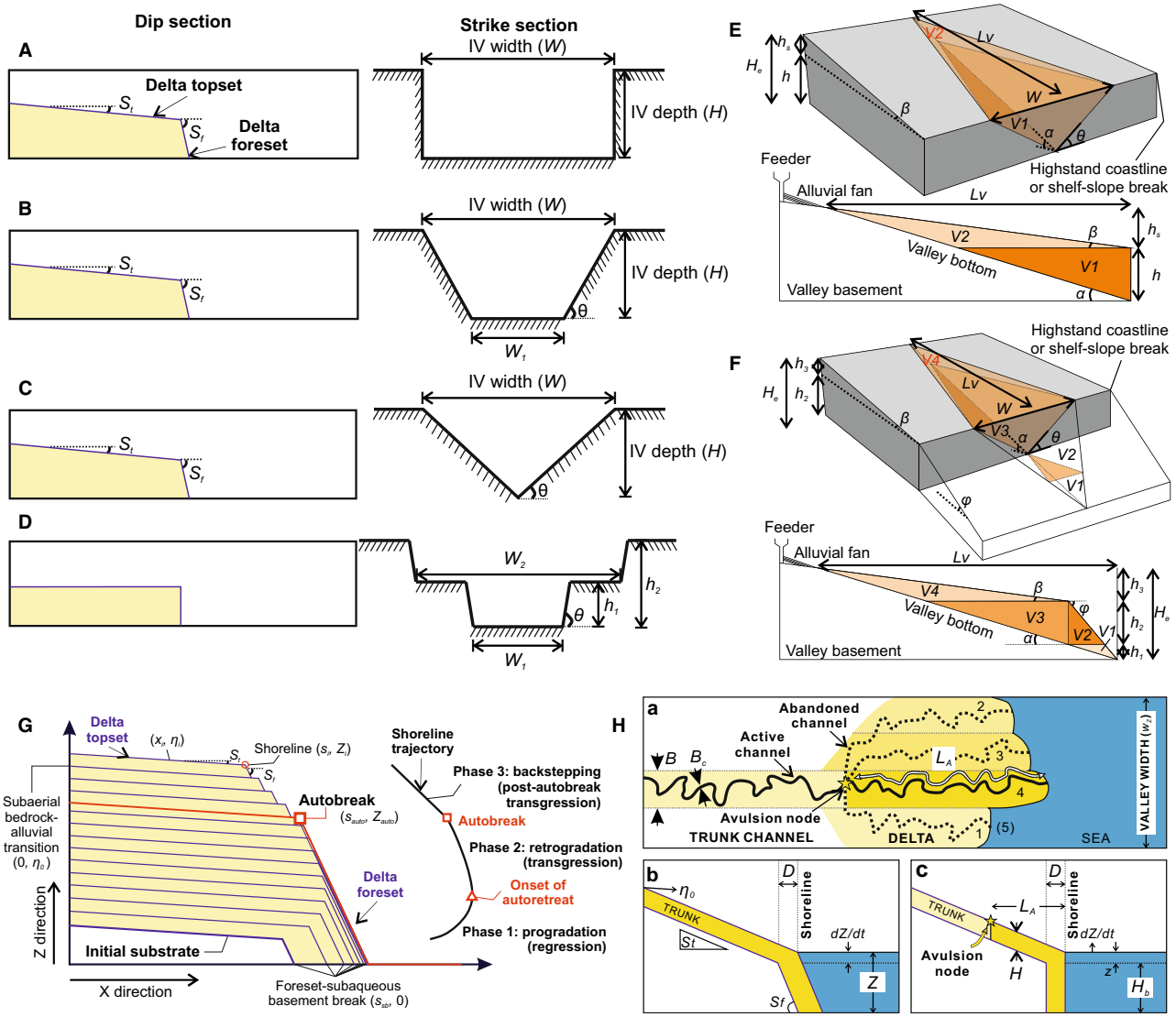

Fig. 1. Conceptualization for the geometric modelling work. (A) to (F) Definition sketch illustrating the valley geometries considered in this work: valleys with a rectangular (A), trapezoidal (B), triangular (C), or terraced strike cross-section (D) and constant morphology in dip direction; valley that deepens and widens seaward (E); and valley that narrows and shallows seaward and landward having its deepest and widest point at some topographic break in slope (F). The in-valley delta geometries are shown in (A) to (D). For valleys with a terraced strike section (D), a flat deltaic topset and vertical foreset are assumed. Cases (E) and (F) are modified after Guerit *et al.* (2020). (G) Schematic diagram illustrating the longitudinal evolution of a delta in response to relative sea-level (RSL) rise. The bold solid red line denotes the surface of the deltaic clinoform at or prior to the attainment of autobreak state. (H) Model conceptualization in plan-view (a) and dip section (c) of the revised backwater-scaled avulsion model to simulate the avulsion timescale of in-valley delta with rising sea level. It shows a trunk channel with a width B_c feeding delta lobes with a width B and a fixed avulsion length L_A determined by backwater effects. (b) Model conceptualization in dip cross-section for the spatially averaged mass-balance model to estimate the avulsion timescale for the entire in-valley river system. Modified after Chadwick *et al.* (2020).

zero, reaching a state termed as 'autobreak' (Muto, 2001). After this state, the configuration of the initial delta front can no longer be retained because of sediment starvation across the shoreline. The delta then switches to an estuary and the shoreline starts to retreat landward. In this work,

these concepts are applied and expanded to models envisaging varying 3D incised-valley geometries. Details on the geometric models simulating shoreline migration patterns for valleys with simple geometries are presented in Supporting Information S1.

Shoreline migration patterns for complex valley geometries

For valleys with complex geometries (Fig. 1E and F), a ratio of the rate of accommodation creation to the rate of sediment supply is employed as a tool for the prediction of the shoreline behaviour (Cross, 1988; Schlager, 1993; Rodriguez *et al.*, 2008) in response to constant rates of RSL rise and sediment supply (cf. Guerit *et al.*, 2020). For a valley that deepens and widens in the seaward direction (Fig. 1E), the model is the same as that presented in Guerit *et al.* (2020). Hence, it is only briefly summarized here. The original model assumes a V-shaped valley with width W, total elevation range of the valley base H_e, horizontal length L_v, valley thalweg gradient α, sidewall slope θ and interfluve slope β ($\beta < \alpha$; Fig. 1E). Building on this model, a new model is developed to account for an additional valley geometry that narrows and shallows seaward beyond the deepest and widest point, near the slope break (Fig. 1F). This new model assumes a doubly tapering V-shaped valley with an interfluve slope β landward of the slope break (either lower coastal-plain or continental shelf) and an interfluve slope φ seaward of the slope break (either inner shelf or continental slope), where $\beta < \alpha < \varphi$ (Fig. 1F). The total elevation range of the valley base H_e is divided into two heights, one between the base of the valley mouth and the slope break, $h_1 + h_2$, and the other between the valley head and the slope break, h_3. The base level, Z, is calculated by the RSL rise rate dZ/dt multiplied by the time t, assuming an initial base level at the height of the valley mouth. When sea level is below the bottom height ($Z < h_1$), the volume available for sediment deposition in the valley is:

$$R = \frac{1}{6}\frac{Z^3\,W}{h_1 + h_2}\left(\frac{1}{\alpha} - \frac{1}{\phi}\right). \tag{1a}$$

When sea level rises above the bottom height and below the slope break ($h_1 < Z < h_1 + h_2$), the volume available in the valley is described as:

$$R = \frac{1}{6}\frac{Z^3\,W}{h_1 + h_2}\left(\frac{1}{\alpha} - \frac{1}{\varphi}\right) + \frac{1}{2}\frac{W}{\varphi}\frac{1}{h_2(h_1 + h_2)}\left[h_2{}^2(h_1 - Z)^2 + h_1 h_2{}^2(Z - h_1) + \frac{1}{3}(h_1 + 2h_2)(h_1 - Z)^3\right] + \frac{(Z - h_1)^3}{3\alpha\theta}. \tag{1b}$$

When the sea level rises above the slope break ($Z > h_1 + h_2$), the volume changes to:

$$R = \frac{1}{6}W\,h_2\,L_v - \frac{1}{6}\frac{(h_1 + h_2 + h_3 - Z)^3\,h_2\,W}{\alpha\,h_3{}^2}. \tag{1c}$$

Hence, the rate of accommodation creation A within the valley during steady sea-level rise can be estimated by dR/dt, representing the volumetric change within the valley in a time step dt. In the current modelling work, the input sediment supply is determined at a rate that can fill the entire valley accommodation in the total time duration T and is calculated by dividing the total valley volume by the total time duration T.

Estimation of the characteristic avulsion timescale

For modelling the dynamics of the characteristic avulsion timescale on the in-valley fluvio-deltaic system in response to RSL rise, only valleys with simple geometries (Fig. 1A to D) are considered. Channel avulsion occurs periodically with a characteristic time that is generally thought to scale with the time required for the fluvial system to aggrade to a critical height (Mohrig *et al.*, 2000; Jerolmack & Mohrig, 2007; Supporting Information S2). In this work, two integrative approaches are employed to approximate the fluvial topset aggradation rate in order to simulate the temporal evolution of the characteristic avulsion timescale on the valley-confined fluvio-deltaic systems (Supporting Information S2; Fig. 1H). First, the avulsion timescale, T_A, for the entire in-valley river system is predicted based on the approximation of the fluvial topset aggradation rate, V_a, through spatial averaging of sedimentation in the cross-valley direction ('spatially averaged mass-balance model', hereafter; SM model; Fig. 1Hb). Second, the avulsion timescale for in-valley deltas is predicted by a revised backwater-scaled avulsion model proposed by Chadwick *et al.* (2020) ('backwater-scaled avulsion model',

hereafter; BA model; Fig. 1Ha and Hc). The BA model constrains fluvial aggradation rate using sediment mass balance for an individual delta lobe over an avulsion timescale while setting delta lobes to a fixed length, L_A, determined by the backwater length, L_b. This is in contrast with the SM model, which accounts for the avulsion of the entire river system (for example, the trunk channel upstream of the delta apex) or on fan deltas whose apex is fixed in space at a feeder-valley outlet (i.e. topographically controlled avulsion; cf. Ganti *et al.*, 2014).

Normalization

To ensure the applicability of the model to a broad range of deltas across different valley geometries, results are normalized by characteristic time and length scales. The shoreline position, s_s, sediment surface elevation, η, and base level, Z, are normalized by the autostratigraphic length scale, L_{auto} (cf. Muto *et al.*, 2007), which is defined as $L_{auto} = q_s/(dZ/dt)$, where q_s represents the rate of sediment supply per unit width. The time, t, and avulsion timescale, T_A, are normalized by the autostratigraphic timescale, T_{auto}, given by $T_{auto} = \frac{{L_{auto}}^2 S_c}{q_s}$, where S_c denotes the channel bed slope, which, for simplicity, in this work is considered equal to the uniform slope of the fluvial topset reach S_t. The shoreline migration rate and aggradation rate in the fluvial topset are both normalized by L_{auto}/T_{auto}. L_{auto} and T_{auto} represent the critical length and time of the fluvio-deltaic system at the attainment of autobreak, respectively, assuming that the entire sediment supply is sequestered uniformly on the delta topset in response to a given RSL rise (cf. Muto *et al.*, 2007). Specifically, in this work, to facilitate comparison across different valley geometries, the width averaged sediment supply, q_s, is determined by the volumetric sediment supply, Q_s, divided by the valley width averaged in cross-section W_N ($q_s = Q_s/W_N$). The cross-section-averaged valley width, W_N, is estimated through the valley strike cross-sectional area, A_V, divided by the total valley height H ($W_N = A_V/H$, detailed in Supporting Information S3 and Fig. S1B).

Model implementation

For valleys with simple geometries (Fig. 1A to D), to isolate the delta response to a RSL rise across the different types of valley shape, the current modelling systematically varies the parameters related to the valley geometries whilst maintaining a uniform strike-oriented cross-sectional area of the inundated valley. This, coupled with constant downdip valley morphology, can ensure the same total magnitude of accommodation creation within the valley over the total duration of infilling, T. In the modelling runs for valleys with simple geometries (Fig. 1A to D), an idealized incised valley is considered, unless otherwise specified for different valley geometries, as would be seen in the inset maps of Fig. 3A to E: a cross-section-averaged valley width $W_N = 4800$ m, a valley height $H = 200$ m and a valley sidewall slope $\theta = 0.1$. The valley length is assumed to be infinite. The following variables are held constant across the model runs: initial base level ($Z_i = 5$ m), sea-level rise rate ($dZ/dt = 5.7E{-}3$ m/year), sediment supply rate ($Q_s = 20\,000$ m^3/year), sediment porosity ($\lambda_p = 0.4$), the prescribed delta geometry (delta topset slope $S_t = 0.01$ and foreset slope $S_f = 0.33$), and total run time ($T = 34\,211$ years). The specific value for the delta topset slope has been chosen herein to ensure achievement of a full cycle of regression, transgression and post-autobreak transgression in the modelling results. Nevertheless, it is acknowledged that this value of deltaic topset slope is larger than what is common for most large lowland deltas in natural systems. Taking this into account, the responses of valley-confined deltas to sea-level rise has also been investigated independently for a range of delta topset slopes ($S_t = 0.01, 0.001$, and 0.0001).

In the modelling runs for valleys with complex geometries (Fig. 1E and F), an idealized incised valley is considered: a maximum valley width $W = 1$ km, a valley height $H = 100$ m, a horizontal valley length $L_v = 1667$ m, a valley thalweg slope $\alpha = 0.06$, a landward interfluve slope $\beta = 0.02$, a seaward interfluve slope $\phi = 90°$ or 0.139 for the two types of complex valley geometries, and a total duration of infilling $T = 100$ kyr. Especially, to explore how the seaward interfluve slope ϕ (Fig. 1F) affects the overall shoreline behaviour, the parameter ϕ has been changed systematically by multiplying or dividing it by 2 whilst keeping other variables constant.

In the modelling run, to simulate the avulsion timescale, the relevant variables are set constant with values typical for large lowland deltas ($H_c = 2$ m, $B_c = 40$ m, $H^* = 0.5$, $L_A = L_b$, $B = 40B_c$).

In the modelling work, input quantities are chosen arbitrarily but ensuring that they are within ranges of observations from late-Quaternary incised valleys (Wang *et al.*, 2019). In particular, interfluve slopes landward and

seaward of slope breaks are chosen in consideration of the gradient range of modern coastal plains, continental shelves and continental slopes (Wang *et al.*, 2019). Nevertheless, within the modelling framework, the aforementioned parameters are readily adjustable.

Physical experiments

Experimental design and data collection

To integrate the results of the above-described numerical models, four scaled physical experiments were conducted. These employed different valley geometries, i.e. valleys with rectangular (Experiments 1 and 4) and triangular cross-sectional shapes (Experiment 2), and constant longitudinal (downdip) morphology, and a V-shaped valley that deepens and widens basinward (Experiment 3; Table 1). Each experiment was conducted on a non-erodible acrylic valley base with a given geometry inserted in a larger flume tank with a flat basin floor ($4.0 \times 0.4 \times 0.4$ m). Water and sediment discharges were imposed at constant rates using a recirculating hydraulic pump and sediment feeder, respectively (Table 1; Fig. 2). Water was dyed blue to capture the shoreline and streamflow. Constant sea-level rise rate was achieved with the use of an additional hydraulic pump (Fig. 2). For each experiment, an 80 : 20 volume ratio in the mixture of crushed walnut-shell sediment and fine quartz sand was used to represent the relative proportions of fine and coarse sediments, respectively (cf. Baumanis & Kim, 2018). Here, the crushed walnut-shell sediment was used as it can increase the bank cohesiveness, and tends to promote the formation and maintenance of deeper single thread channels compared to other non-cohesive sediment mixtures (Sheets *et al.*, 2007). All experiments were conducted under the subcritical flow condition (Froude number $Fr < 1$) to approximate conditions in large lowland deltas. Each experiment (except for Experiment 3) started with a self-organized delta (Supporting Information S4; cf. Sheets *et al.*, 2007; Martin *et al.*, 2009) developing on an initial sediment substrate that was either 1 m or 2 m long (Table 1; Fig. 2). The experiments ended after a total run time of 55 h. Experiment 3 began without an initial delta in the 2 m long valley. Details on the experimental set up can be found in Supporting Information S4.

Overhead images of deltaic evolution were taken every minute and utilized to identify the position of shoreline and avulsions (Fig. 2). Bed

Table 1. Experimental conditions for the experiments conducted in this work.

Experiment	Experiment 1	Experiment 2	Experiment 3	Experiment 4
	Rectangular	Triangular	V-shaped	Rectangular
Valley geometry	Valley width $W = 0.2$ m; valley depth = 0.4 m; horizontal valley length $L_v = 4$ m	Valley width $W = 0.4$ m; valley depth = 0.15 m; horizontal valley length $L_v = 2$ m; valley sidewall slope $\theta = 0.75$	Valley width $W = 0.4$ m; valley depth = 0.106 m; horizontal valley length $L_v = 2$ m; valley sidewall slope $\theta = 0.75$; valley thalweg slope $\alpha = 0.053$	Valley width $W = 0.4$ m; valley depth = 0.4 m; horizontal valley length $L_v = 4$ m
Initial substrate	1 m long; 1% slope	1 m long; 1% slope	None	2 m long; 1% slope
Q_w (cm^3/min)	1000	1000	1000	1000
Q_s (cm^3/min)	2	2	2	2
dZ/dt (cm/min)	0.0016	0.0015	0.0018	0.00068
Fr (−)	0.3	0.3	0.31	0.3
Run time (h)	55	55	55	55

Q_w denotes volumetric water discharge; Q_s denotes volumetric sediment discharge; dZ/dt denotes relative base-level rise rate; Fr denotes Froude number of the normal flow. Fr is computed using the following relation: $Fr = U/\sqrt{gh_n}$, where g is the acceleration due to gravity, h_n is the channel depth of the normal flow, U is the depth-averaged flow velocity. The depth-averaged velocity is estimated by the ratio of the water discharge and the channel cross-sectional area, which is determined by the channel width and flow depth (h_n). This is complemented by the conversion based on the water surface velocity reported using the surface float video (see text for details).

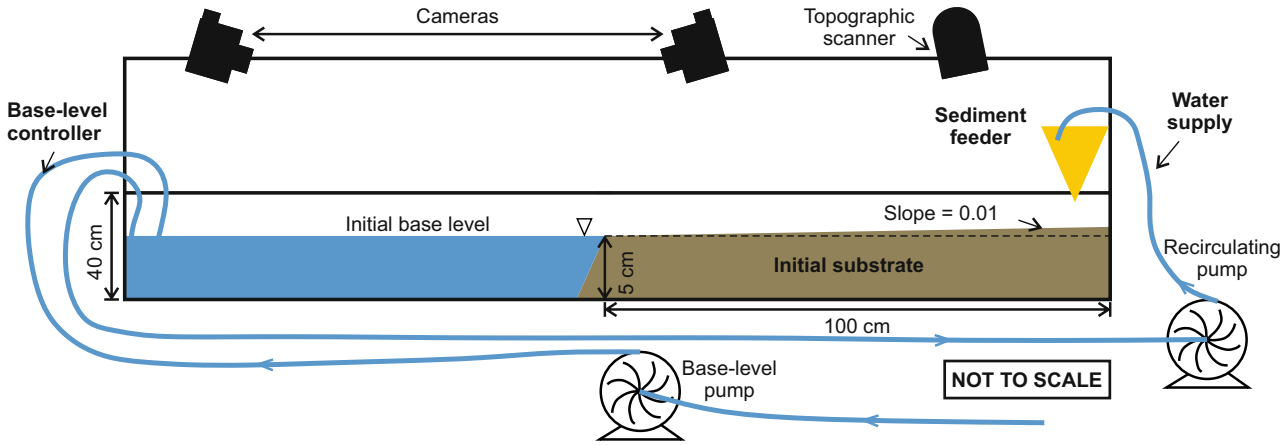

Fig. 2. Experimental arrangement of the physical experiments along a side view. An initial substrate with a topset slope of 0.01 was prepared for Experiments 1, 2 and 4, whereas no sediment was used for Experiment 3.

topography was monitored every hour with a laser scanner (5 mm horizontal resolution, 2 mm vertical resolution). Water surface velocity was measured by digitizing the pathways of surface floats with time imaged in a video, which was subsequently converted to a mean depth-averaged velocity by multiplication by a factor of 0.8 (cf. Matthes, 1956; Leopold *et al.*, 1964; Graf, 1998; Table 1). At the end of each experiment, the final deposits of the delta topset were sliced along the strike direction serially at an interval of 30 mm. Each section was then photographed.

Experimental data analysis

Temporal evolution of the shoreline in each experiment was captured in two integrative ways: (i) by identification of the shoreline by tracking the boundary between the blue-dyed water and brown sediment surface in the orthorectified, time-lapse overhead images, which was undertaken in Adobe Photoshop CS; and (ii) by mapping the location of the delta topset–foreset break using the time-series topographic scans.

Identification of times for the channel avulsions were undertaken manually using overhead time-lapse images. Following previous work (e.g. Ganti *et al.*, 2016), avulsions were identified at the establishment of a totally new channel that captured most of the flow during a subsequent flow event, and that led to a complete or partial abandonment of the parent channel. The avulsion time was recorded as the time at which the levée of the parent channel was breached.

Deposition and erosion on the delta topset were monitored by the measurements of the bed elevation during the experimental run via the topographic scanner. To visualize these processes more clearly, a panel of synthetic stratigraphy along the longitudinal axis of the valley for each experiment was constructed. This was achieved by stacking digital elevation models from the topographic scans and clipping the previous topography during episodes of erosion (Straub *et al.*, 2012). To denoise the data related to the 3D bed surface topography, a moving-window average filter with a non-overlapping window size of 1.5 cm was utilized. The elevation data deleted during the former filtering procedure were subsequently substituted by linear interpolation (cf. Ganti *et al.*, 2016).

To explore the linkage between surface morphodynamics and subsurface fluvial stratigraphy for deltas confined by incised valleys, strike-oriented synthetic stratigraphic panels of channel deposits were generated for each experiment. These were achieved by mapping channel locations from the overhead time-lapse images (every 30 min) and stacking them vertically based on the limited scanned topographic data (every 1 h). The generalized workflow mainly followed the method presented by Steel *et al.* (2022) and is detailed in Supporting Information S5. Nevertheless, due to the limited grain-size variation of the sediment mixture in the experiments, the sliced sections of the final deposits do not exhibit well-developed stratigraphy and therefore were merely used as a complement to the constructed strike-oriented synthetic stratigraphy.

Trend lines of the experimental data points over time (for example, mean shoreline position and delta-top aggradation rate) were produced in MATLAB using the built-in function

trenddecomp. This function detects long-term trends in a vector of uniformly spaced data using singular spectrum analysis, which assumes an additive decomposition of the data and which is typically useful when the periods of seasonal trends are unknown.

RESULTS

Geometric modelling

Shoreline migration patterns for simple valley geometries

The evolution of in-valley deltas (dip cross-sectional view in Fig. 3A to E) and associated shoreline migration patterns (shown as red shoreline trajectories in Fig. 3A to E and shoreline migration rates in Fig. 3F to J) with rising RSL are simulated under the conditions of constant rates of RSL rise and sediment supply for simple valley geometries.

Across different valley geometries (Fig. 3A to E), the shoreline trajectory commonly exhibits an overall convex-seaward curve, with two recognizable points: the maximum seaward advance point (s_M, Z_M) and the autobreak point (s_{auto}, Z_{auto}). These two points respectively represent: (i) the turning point at which the shoreline advance is halted and the shoreline starts to retreat landward; and (ii) the point after which the initial delta front becomes abandoned due to sediment starvation at the shoreline and the delta switches to an estuary (Fig. 1G; cf. Muto, 2001). The delta develops with an initial phase of progradation under decreasing shoreline advance rates, until reaching a shoreline autoretreat phase, and eventually switches to a post-autobreak or backstepping phase. Nevertheless, the position and timing of the landward turnaround of the shoreline migration (i.e. autoretreat), the distinct change of the delta geometry in the retreat phase (i.e. autobreak) and the retreat rates in the post-autobreak phase are systematically different across different valley geometries (Fig. 3A to E).

For the valley with the rectangular cross-section (Fig. 3A), the autobreak state is never attained over the experimental duration of infilling, T. The deltaic foreset is never abandoned; instead, it continues to accrete whilst the topset shrinks. It can be inferred that if the RSL rise persists for a long enough time and the valley is sufficiently deep, the topset will eventually disappear and the entire system will be drowned (cf. 'autodrowning' of Tomer *et al.*, 2011). Nevertheless, the autobreak event occurs for valleys with trapezoidal (Fig. 3B) and triangular (Fig. 3C) cross-sections. Compared to the modelling results for valleys with the rectangular cross-section (Fig. 3A), outputs for the valley with the triangular cross-section (Fig. 3C) indicate a more prominent convex-seaward shoreline trajectory. Maximum seaward advance and autobreak occur more rapidly at locations that are respectively more seaward and lower ($s_M = 0.791$ versus $2.320; Z_M = 0.0687$ versus 0.0237). The positions of maximum seaward advance and autobreak nearly overlap (Fig. 3C), i.e. the delta undergoes the autobreak as soon as the landward retreat of the shoreline commences. Hence, only a short or negligible span of the shoreline trajectory embodies the autoretreat phase (retrogradational phase in Fig. 1G). For the valley with the trapezoidal cross-section (Fig. 3B), the positions and the timings of maximum seaward advance and autobreak fall between those of the runs with the rectangular and triangular valley cross-sections ($s_M = 1.097; Z_M = 0.0462; s_{auto} = 0.986; Z_{auto} = 0.698$). Furthermore, compared to the modelled valley with the triangular cross-section (Fig. 3C), the position of the autobreak for the valley with the trapezoidal cross-section (Fig. 3B) lies further away, both vertically and horizontally, from the position of the maximum seaward advance. Therefore, a larger fraction of the shoreline trajectory is represented by the autoretreat phase.

Despite the general trend (i.e. initial progradation, autoretreat after the maximum shoreline advance and backstepping after the autobreak; Fig. 1G) shown in the shoreline trajectory (Fig. 3A to E) being nearly the same across the modelling runs with different valley geometries, the shoreline migration rates vary markedly across the runs (Fig. 3F to J). For the valley with the triangular cross-section (Fig. 3C and H), the shoreline advances with an initially rapid but ever decreasing rate in the progradational phase, then undergoes a gradually decelerating retreat during the very short autoretreat phase, and subsequently an abrupt increase in retreat rate due to the autobreak, which ultimately decreases steadily to approach zero during the backstepping phase. For the valleys with the rectangular and trapezoidal cross-sections (Fig. 3F and G), the overall absolute rates over the progradation and retrogradation stages are commonly much slower than those in the valley with the triangular cross-section.

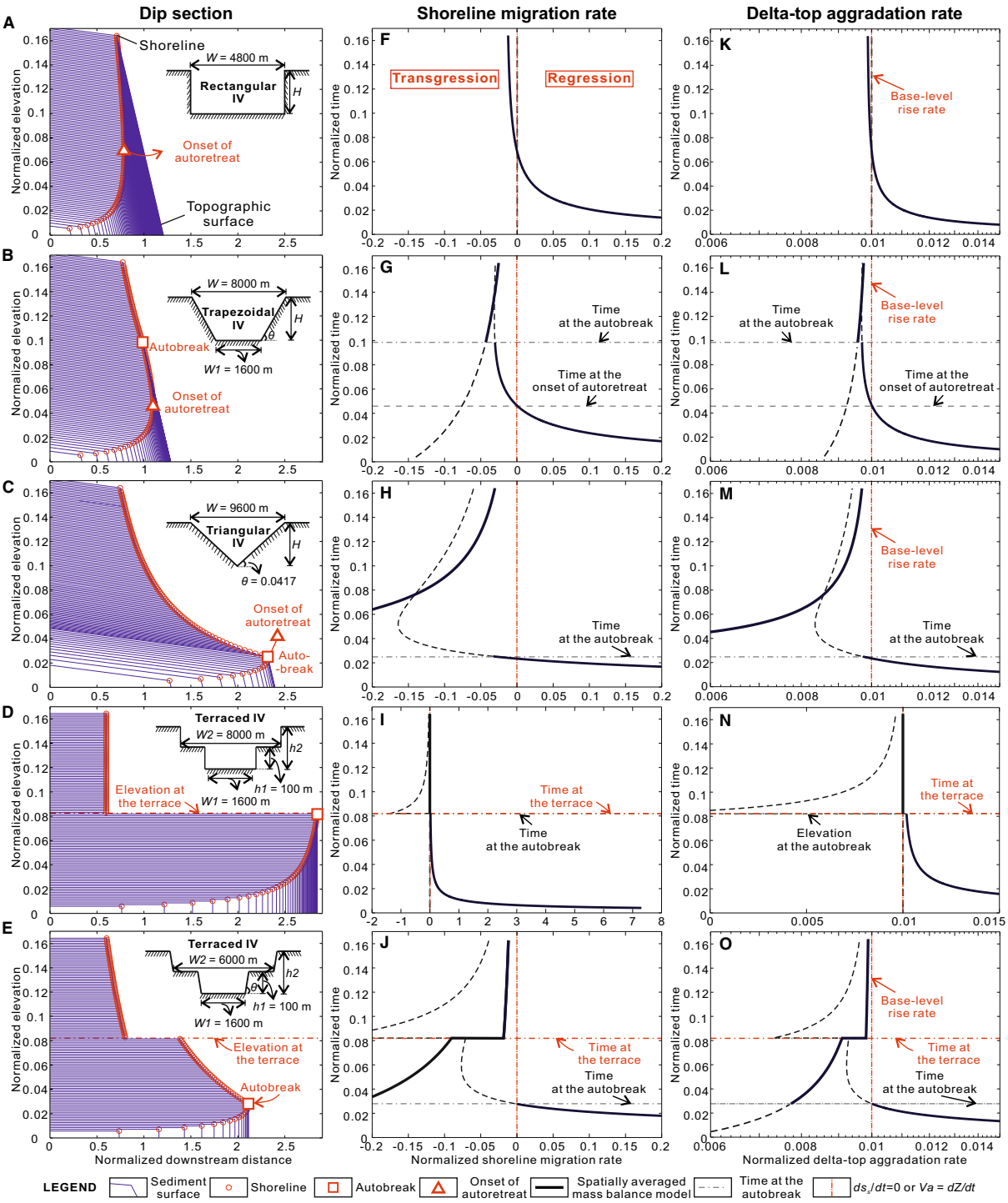

Fig. 3. Modelling results of longitudinal delta evolution (A) to (E), non-dimensional shoreline trajectory (A) to (E), shoreline migration rate (F) to (J) and delta-top aggradation rate (K) to (O) for different valley geometries (simple valley geometry) under conditions of constant rates of base-level rise and sediment supply. Inset diagrams in (A) to (E) depict the corresponding valley geometries in strike cross-section. In (A) to (E), total run time is 34 211 years and topographic surfaces are drawn every 300 years. In (F) to (O), model outputs are indicated as black thick solid lines. Different models are employed for phases before and after the autobreak. Outputs from models that are not applicable to either phase are shown as black thin dashed lines.

For the valleys with terraced cross-sections (Fig. 3D and E), two scenarios are considered by setting the valleys with vertical or inclined sidewalls. For the valley with the vertical valley walls (Fig. 3D), the delta initially progrades at a rapid but ever decreasing rate. When the sea level floods the terraces, the delta abruptly retreats landward (cf. Rodriguez *et al.*, 2005) and starts to aggrade vertically. For the valley with the inclined sidewalls (Fig. 3E), the autobreak is attained below the bottom terrace ($s_{auto} = 2.110; Z_{auto} = 0.0280$). The shoreline initially advances seaward very rapidly, and then commences to retreat rapidly during the post-autobreak phase. As sea level continues to rise and inundates the relatively flat fluvial terraces, the width inside the valley suddenly increases, leading to a sudden landward shift of the shoreline (cf. Rodriguez *et al.*, 2005). Notably, the rates of shoreline retreat for times when sea level is above the terrace are systematically slower than those for times when sea level is below the terrace and after the autobreak is attained (Fig. 3J). This likely happens because, after major shoreline retreat, the in-valley depositional system becomes much wider laterally but shorter along the dip direction, and only survives over the shallow flooded terraces and the previous delta topset. Under these conditions, for a given sediment supply rate, the sediment mass balance dictates that the in-valley depositional system will retreat at slower rates to maintain this newly developed geometry when sea level is above the terrace, compared to times when sea level is below the terrace.

Shoreline migration patterns versus deltaic geometries for simple valley geometries

To compare the responses of valley-confined deltas that have different geometries to sea-level rise, a range of delta topset slopes (S_t) are considered: $S_t = 0.01, 0.001$ and 0.0001 (Fig. S2). As the deltaic topset slope decreases in the modelling runs, the shoreline trajectory tends to feature a more prominent convex-seaward geometry, and the maximum seaward advance and autobreak points occur at more seaward and lower positions. Nevertheless, the prominence of these features varies significantly across different valley geometries. For the valley with a rectangular cross-section, the maximum seaward advance of the shoreline is located at a slightly higher position without a significant horizontal offset as S_t increases. For the valley with a trapezoidal cross-section, the shoreline trajectories for deltas with $S_t = 0.001$ and 0.0001 exhibit a slightly more prominent convex-seaward geometry compared to the case with $S_t = 0.01$; the maximum seaward advance and the autobreak points are attained at more seaward and lower positions with a lower S_t. For the valley with a triangular cross-section, the shoreline trajectories for different topset gradients show changes similar to those observed for other valley geometries, but indicate a much more striking separation.

Avulsion timescales for simple valley geometries

Considering the importance of delta-top aggradation rates in the estimation of avulsion timescale of the in-valley fluvio-deltaic system, changes in delta-top aggradation rate with rising sea level are simulated for different valley geometries (Fig. 3K to O). Because delta-top aggradation rate scales positively with shoreline migration rate (Eq. S11), the model produces trends for the variation of delta-top aggradation rate over time (Fig. 3K to O) similar to the variation of shoreline migration rate with rising sea level (Fig. 3F to J). Detailed descriptions of the dynamic relationship between delta topset aggradation rate and rising sea level are presented in Supporting Information S6.

The characteristic avulsion timescales of the in-valley fluvio-deltaic system with rising sea level is examined separately for results of the BA model (Fig. 1Ha and 1Hc; orange solid lines in Fig. 4) and SM model (Fig. 1Hb; black solid lines in Fig. 4). Both models produce qualitatively similar trends prior to the autobreak phase: the avulsion timescale increases (i.e. the avulsion frequency decreases) with RSL rise. This is due to the fact that delta topset aggradation progressively decreases in response to the progressive increase in the topset area. Nevertheless, the BA model predicts systematically more frequent avulsion (i.e. shorter avulsion timescale) compared to the SM model. Possibly this is due to the assumption made in the BA model (Chadwick *et al.*, 2020), which sets the trunk channel upstream of the avulsion node to: (i) aggrade only during the construction of the first delta lobe; and (ii) be stationary rather than migrating laterally to fill the river basin (Fig. 1Ha and 1Hc). Therefore, more time is required to aggrade the topset between avulsions in the SM model compared to the BA model.

The BA model predicts avulsions to become more frequent during the backstepping phase,

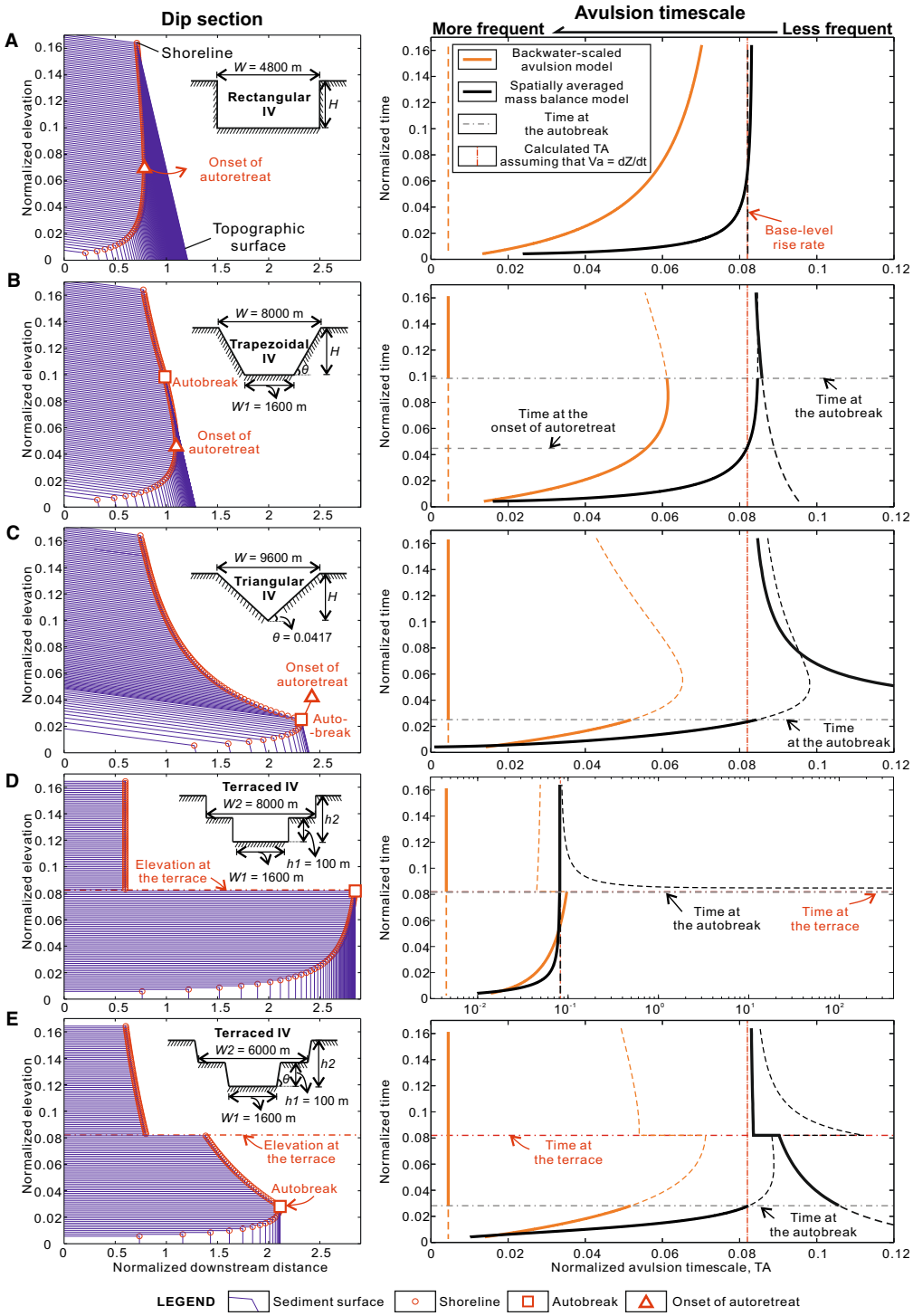

Fig. 4. Modelling results on non-dimensional characteristic avulsion timescales of in-valley fluvio-deltaic systems associated with different valley geometries (simple valley geometry). For reference, the longitudinal delta evolution for different valley geometries is shown on the left-hand side. On the right-hand side, model outputs are reported. Black solid lines refer to the modelling results from the spatially averaged mass-balance model, whereas orange solid lines refer to the modelling results from the revised backwater-scaled avulsion model. For reference, the avulsion timescales for the entire river system simulated by the spatially averaged mass-balance model assuming delta-top aggradation rate equalling base-level rise rate ($V_a = dZ/dt$) are indicated as vertical dashed-dotted red lines. Different models are employed for phases before and after the autobreak. Outputs from models that are not applicable to either phase are shown as thin dashed lines.

yet it considers a constant avulsion timescale ($T_A = 0.00435$) with rising sea level, regardless of valley geometry (Fig. 4). One of the important findings in Chadwick *et al.* (2020) and Chadwick & Lamb (2021) is that sea-level rise causes river avulsions at progressively landward-retreating locations relative to the transgressing shoreline set by backwater hydrodynamics; therefore, the lobe length does not change during shoreline retreat. Hence, due to (i) the fixed delta lobe length set by backwater hydrodynamics and prescribed delta lobe width, and (ii) the constant sediment supply rate prescribed in the model, a constant aggradation rate and therefore a constant avulsion timescale of a single lobe can be expected during the backstepping phase.

In contrast, the SM model (black solid lines in Fig. 4) predicts different patterns of avulsion frequency for different valley geometries during the backstepping phase. For the valley with the rectangular cross-section (Fig. 4A), the normalized avulsion timescale converges to $T_A = 0.0820$ with sea-level rise. This value is equivalent to the expected avulsion timescale for conditions of aggradation rate equalling to the rate of sea-level rise. This happens because, under these conditions, nearly all of the sediment is partitioned to the delta topset rather than the foreset, and the creation of accommodation remains constant over time for a given RSL rise rate due to the rectangular valley geometry. This, in turn, leads to vertical aggradation of the delta at a rate determined mainly by the rate of RSL rise. For the valley with the triangular cross-section (Fig. 4C), the SM model predicts that the onset of autobreak is associated with much less frequent avulsions, the frequency of which subsequently increases during the ensuing RSL rise. Given that avulsion frequency scales positively with aggradation rate, the abrupt decrease in avulsion frequency at the autobreak is due to the interplay of the abrupt changes in sediment partitioning between the delta topset and foreset at the autobreak and the upward widening of the valley with RSL rise. This results in faster shoreline retreat and, in turn, lower delta topset aggradation. For the valley with the trapezoidal cross-section (Fig. 4B), changes in avulsion timescale over time simulated by the SM model exhibit a similar trend to those seen in the model for the valley with the triangular cross-section (Fig. 4C), except for a slight increase in avulsion timescale at the onset of autobreak compared to the former phase and a slower decrease during the backstepping phase.

For the valleys with the terraced cross-section, several outcomes are seen when the sea inundates the flat terraces: (i) the in-valley depositional system undergoes the backstepping phase both before and after the inundation of the terrace; (ii) the in-valley depositional system progrades both before and after the flooding of the terrace; (iii) the in-valley depositional system undergoes a transition phase when crossing the terrace (a transition between Phases 1, 2 and 3 shown in Fig. 1G, i.e. progradation to autoretreat or backstepping; autoretreat to backstepping). The way the in-valley depositional system evolves before the terrace is flooded, and in particular whether the first backstepping episode will occur or not, is mainly determined by the ratio of accommodation creation to the initially assigned sediment supply. If the rate of sediment supply is sufficiently high, the delta will keep prograding and backstepping will not occur until sea level floods the terrace. For the case shown in Fig. 4E, the in-valley depositional system already starts to experience a backstepping phase before sea level rises above the valley terrace. Over the backstepping phase, the SM model predicts a more frequent avulsion when sea level is above the terrace compared to times when sea level is below the terrace. Instead, the BA model predicts no change in avulsion timescale when sea level is above the terrace. Modelling results of the SM model might be explained by the fact that as the in-valley depositional system develops on a shallow terrace during the backstepping phase, it tends to take advantage of the shallow water depth on the terrace and the drowned delta top, leading to higher fluvial topset aggradation rates and hence more frequent avulsions.

The influence of the valley terrace on a prograding delta could also be predicted. For the SM model, because of valley or bay widening, when the flat terraces are flooded, the progradation rate of the entire river system decreases, which in turn induces decreased aggradation rate on the fluviodeltaic topset and less frequent avulsions of the entire river system (for example, Figs 3D, 3I, 3N and 4D). For the BA model (Fig. 4D and E), when the sea inundates the flat terrace, avulsion of a single delta lobe tends to be more frequent compared to times when sea level is below the terrace. An individual delta lobe is expected to prograde more rapidly over the inundated terrace surface due to the shallow water depth on the terrace. Consequently, this leads to higher delta topset aggradation and more frequent avulsion, even

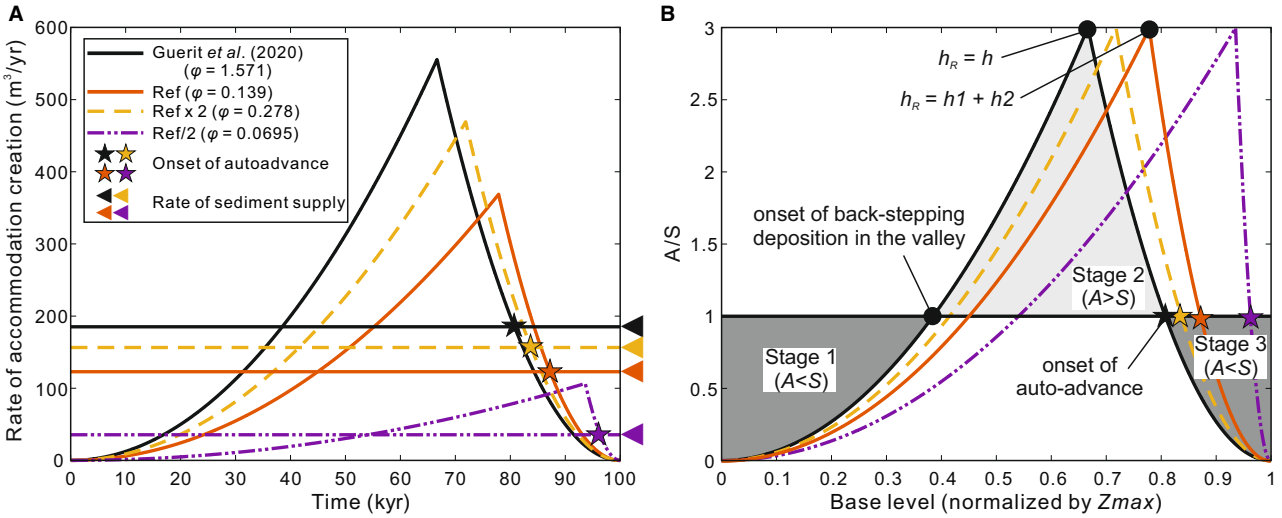

Fig. 5. Impact of the valley geometry on variations of rates of accommodation creation (A) and sediment supply (S) during the inundation of an incised valley (complex valley geometries) under conditions of steady base-level rise and constant sediment supply. (A) Variations of absolute rates of accommodation creation and sediment supply over time during the valley infilling. (B) Variations of ratio of rates of accommodation creation and sediment supply (A/S) during the valley infilling. Base level herein is normalized by the final base level (Z_{max}) at the end of the valley filling. Red solid curves refer to the model for a valley that narrows and shallows seaward and landward, and with a valley thalweg slope $\alpha = 0.06$, a landward interfluve slope $\beta = 0.02$, a seaward interfluve slope $\varphi = 0.139$, a valley maximum width $W = 1$ km, a valley height $H = 100$ m, a valley horizontal length $L_v = 1667$ m and a total time duration of infilling $T = 100$ kyr. Dashed yellow lines and dotted-dashed purple lines refer to models in which the seaward interfluve slope φ was multiplied or divided by 2, respectively, keeping the other parameters unchanged. Black solid lines refer to the model for a seaward deepening and widening valley proposed by Guerit *et al.* (2020). Stars indicate the onset of auto-advance. Triangle on the right of the graph and horizontal solid lines in (A) indicate the rate of sediment supply.

though lobe switching may become less frequent in the deeper part of the valley.

Shoreline migration patterns for complex valley geometries

For valleys with complex valley geometries (Fig. 1E and F), a ratio of rate of three-dimensional accommodation creation (A) to rate of volumetric sediment supply (S) is used to approximate the shoreline behaviour (Fig. 5; cf. Guerit *et al.*, 2020). Under the conditions of constant RSL rise and sediment supply, three distinctive A/S regimes occur during the inundation of the valley (Fig. 5B). During stage 1, the rate of accommodation creation, A, within the valley increases as the sea-level rises, but A is always smaller than S, which leads to progradation, i.e. shoreline advance. During stage 2, A increases and then decreases because of the variation in valley geometry when the sea-level rises above the shelf-slope break, but A is always larger than S, which leads to retrogradation, i.e. shoreline retreat. During stage 3, with a further increase in the sea level, A decreases gradually to the point where A is smaller than S, which induces the resumption of progradation, albeit in the overall context of sea-level rise. This condition at stage 3 is termed 'auto-advance' by Guerit *et al.* (2020).

For valleys with the geometry that narrows and shallows both seaward and landward from the deepest and widest point near the slope break (Fig. 1F), the seaward interfluve slope ϕ, appears to exert an important control on: (i) the absolute rates of accommodation creation within the valley; and (ii) the occurrence and duration of the aforementioned three stages (i.e. stage 1 when $A < S$, stage 2 when $A > S$, and stage 3 when $A < S$; Fig. 5B) during valley inundation (Fig. 5). A lower seaward interfluve slope tends to cause lower rates of accommodation creation within the valley and delays the onset of stage 2 and auto-advance. Therefore, the duration of stage 1 tends to be longer and hence might result in thicker deposits of the basal progradational stratigraphy within the valley. The auto-advance in the scenarios with low interfluve slopes (purple lines in Fig. 5) is

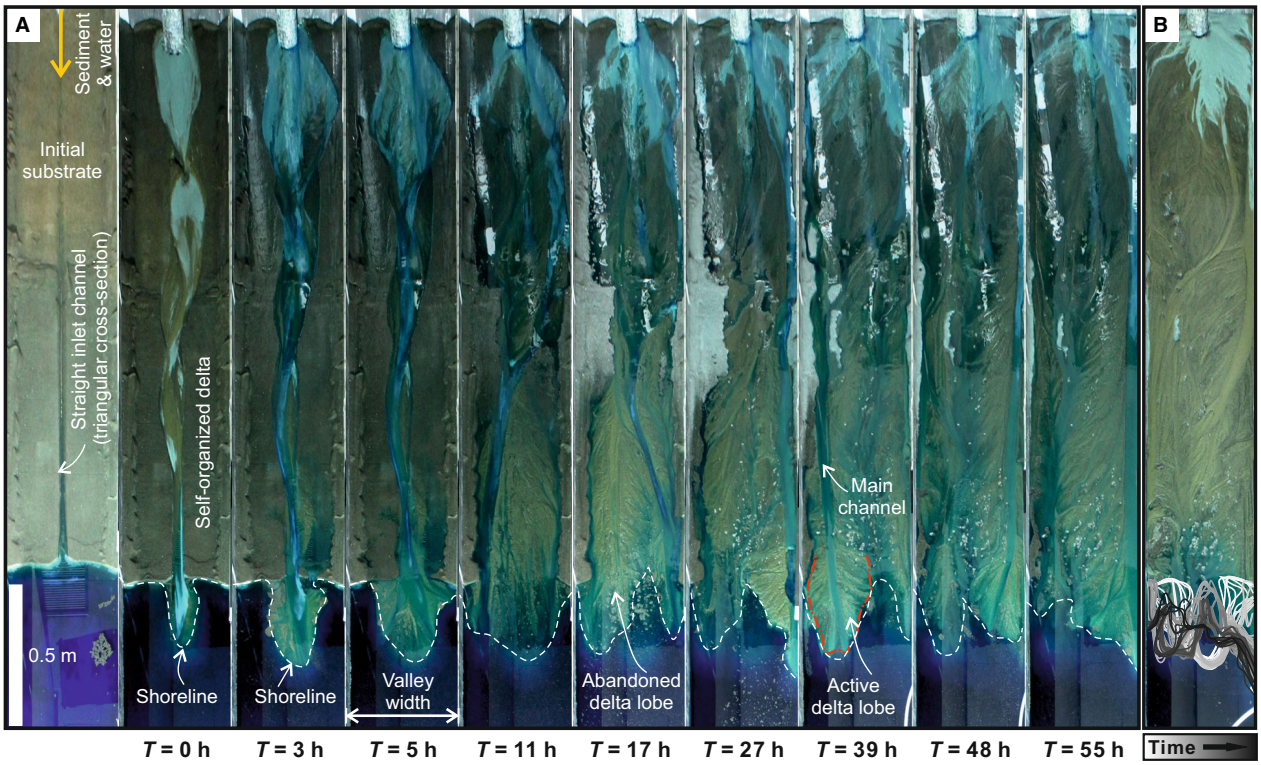

Fig. 6. Example overhead images of the physical experiments. (A) Set of overhead pictures depicting delta growth throughout Experiment 4. The prepared initial substrate with an in-dredged channel at the axis of the valley is shown. T denotes the time when the picture was taken since the formation of the self-organized delta, which is considered as the starting point of the experimental run. (B) Overhead image showing the temporal evolution of the shoreline over the course of Experiment 4, colour-coded according to time.

extremely limited in duration and magnitude. Nevertheless, the durations of stage 2 (retrogradational stratigraphy) are similar across scenarios with different seaward interfluve slopes, all covering *ca* 42% of the total duration of valley filling. Detailed sensitivity analysis of the model outputs to the interfluve slope is presented in Supporting Information S7. Overall, the results shown in Fig. 5 emphasize the importance of accounting for down-dip variations of valley geometry, especially interfluve gradients.

Physical experiments

Surface observations of the experiments

Overall, across the experiments, after an initial period of sheet-like flow, the flow became channelized, and the delta grew via repeated avulsions (Fig. 6A). Over time, the channelization of the flow became increasingly prominent. This is possibly due to decreased aggradation rate with rising sea level arising from decreased progradation rate of the delta over time. Annotated videos of the experiments are presented in Movies S1 to S4.

Shoreline kinematics under rising sea level

Based on the overhead time-lapse images, the shoreline position (i.e. distance from the sediment feeder to the shoreline; Fig. 6B) was captured every hour for each experiment, the mean value of which was subsequently calculated (Fig. 7A). In Experiment 1, the mean shoreline position is observed to generally advance seaward at relatively slow and decelerating rates during the experimental run, with the mean value of shoreline position varying from *ca* 100 to 120 cm (Fig. 7A). The geometric model corresponding to this experiment (dash-dotted line in Fig. 7A) predicts a trend in temporal evolution of the shoreline position similar to the experimental observations, but systematically overpredicts the shoreline position (dashed line in Fig. 7A). Compared to Experiment 1, Experiment 2 is observed to feature a faster shoreline

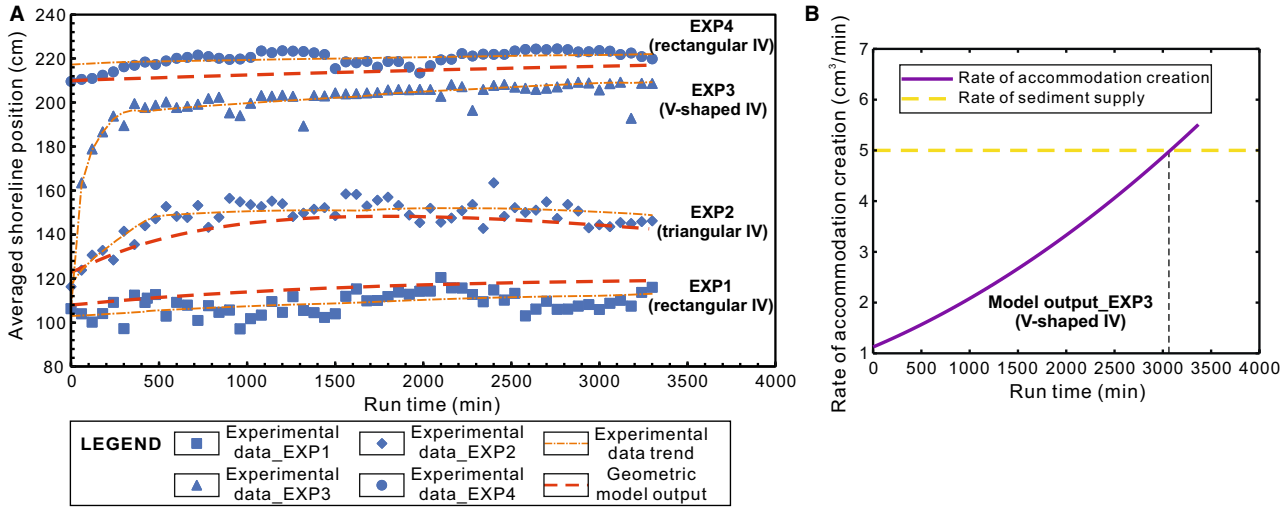

Fig. 7. (A) Temporal evolution of observed and predicted mean shoreline position during the experimental run for Experiments 1 to 4. To facilitate comparison, only the shoreline position recorded every hour is considered herein, which was measured 10 min after the flow was turned off. For Experiments 1, 2 and 4, the shoreline position predicted by geometric modelling is indicated as red dashed lines in (A). Note that deposit compaction and water evaporation produced some conspicuous drops in the experimental mean shoreline position curve (for example, 2460 min for Experiment 2; 1260, 2280 and 3120 min for Experiment 3; 1980 min for Experiment 4). This is an artefact of long pauses during the experiments, but they are recovered quickly after the restart of the experiments. (B) Modelled output for the variation of accommodation creation rate A and input sediment supply rate S in Experiment 3.

progradation in the initial phase of the experiment (mean shoreline position varying from 116 cm at 0 min to 153 cm at 720 min). This is possibly due to the smaller space available for sedimentation in the lower part of the valley with a triangular cross-section. Subsequently, a nearly static shoreline is established from 720 to 1980 min, followed by slow shoreline retreat from 1980 min. The geometric model corresponding to this experiment shows a relatively slower shoreline progradation at the beginning of the model run and an earlier onset time of the shoreline autoretreat at 1500 min, compared to the experimental observations (dashed lines in Fig. 7A). In Experiment 3 (Fig. 7A), the observed mean shoreline initially progrades at an even faster rate than that in Experiment 2 (mean shoreline position varying from 160 cm at 0 min to 198 cm at 420 min), but then slows at gradually diminishing rates. No systematic landward migration of the shoreline during this experiment is observed. Nevertheless, the geometric model corresponding to this experiment predicts a short period of shoreline retreat at the end of the model run (from 3060 to 3300 min; Fig. 7B). In Experiment 4, the mean value of the shoreline position is observed to vary little over the duration of the experiment, which changes from 210 to 224 cm (Fig. 7A). The geometric model corresponding to this experiment predicts a similar trend to the experimental observations, but indicates a systematically closer shoreline position from the sediment source across the experiment (dashed lines in Fig. 7A).

Additionally, the deltaic topset–foreset break can be taken as a shoreline proxy in the stacked digital elevation models along the valley axis (Fig. 8A to C). The shoreline trajectories reconstructed by this approach indicate a trend similar to the one shown in the geometric model outputs for Experiments 1 and 2 (Figs 7B, 8D and 8E). Detailed comparison between the observed shoreline trajectory and that shown in the geometric model outputs is presented in Supporting Information S8.

Overall, the first-order shoreline migration patterns observed over the course of Experiments 1 to 4 are captured by the geometric models (Fig. 7). Discrepancies between experimental observations and numerical model predictions (Fig. 7) are attributed to the following: (i) decoupling of the shoreline and the deltaic topset–foreset break (which was treated as equivalent to the shoreline in the geometric model) due to the drowning of the delta topset subject to RSL rise;

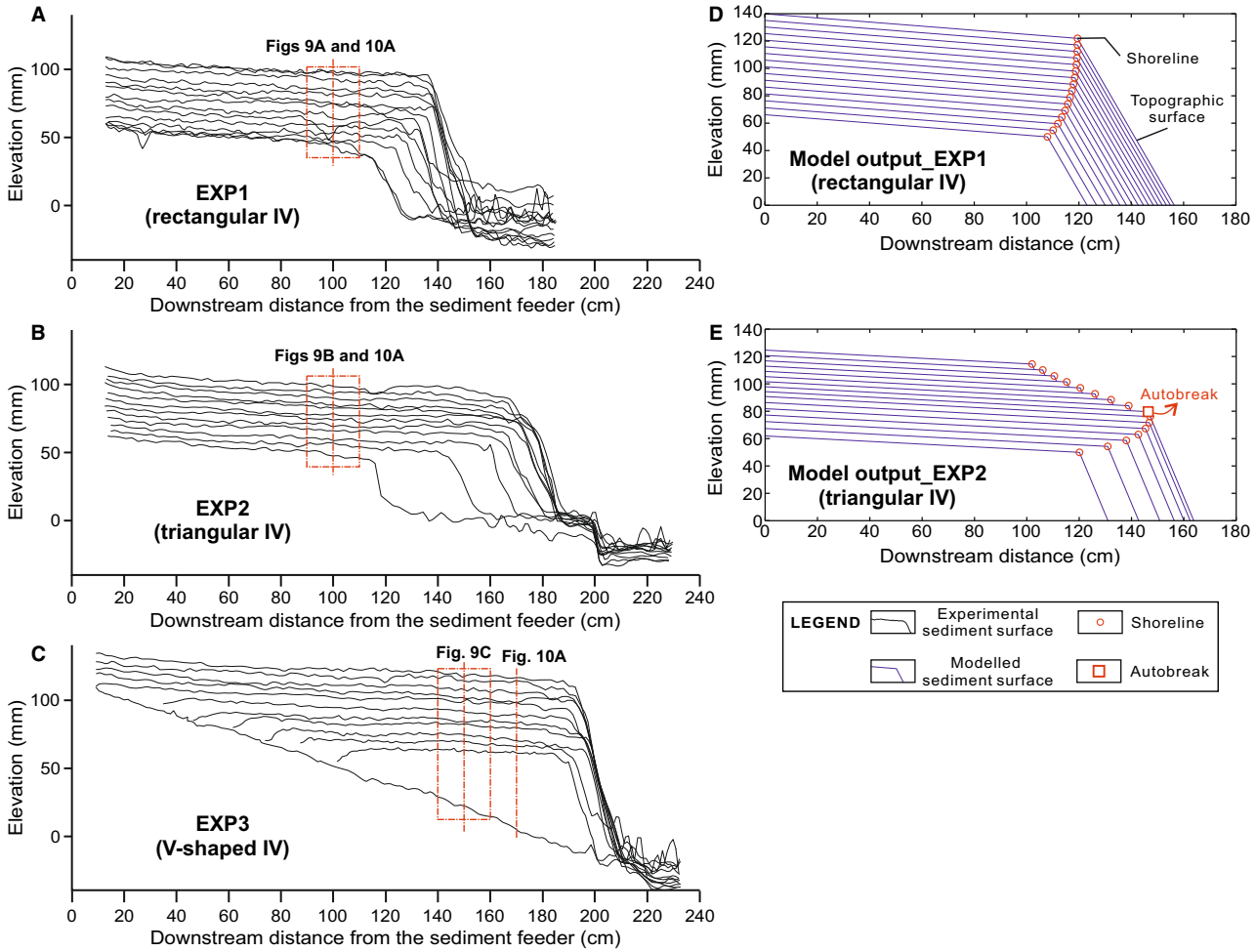

Fig. 8. Dip-oriented synthetic stratigraphic panels along the centreline of the flume for Experiments 1 to 3 (A) to (C), and modelled outputs of corresponding dip-oriented profiles of bed surface elevation for Experiments 1 and 2 (D) and (E). Input parameters for the geometric modelling are set to constant, representative for the current physical experiments. Synthetic stratigraphic panels in (A) to (C) are generated by stacking digital elevation models every 5 h.

and (ii) lack of consideration of the detailed 3D sediment transport dynamics of the valley-confined fluvio-deltaic system (for example, sediment storage and release on the delta topset in time and space; cf. Kim *et al.*, 2006) during RSL rise in the geometric model.

Delta-top aggradation rate and avulsion timescale under rising sea level

To integrate the results simulated by the geometric model in predicting delta-top aggradation rate with rising sea level, the local sedimentation rate on the delta topset is estimated. This is derived from the time-series topographic scan data at a specific location along the valley axis for each experiment (Fig. 9A to C). The chosen sites are located at 100 cm downstream from the feeder along the valley centreline for Experiments 1 and 2, and at 150 cm for Experiment 3 (red vertical dashed lines in Fig. 8A to C). The local sedimentation rate on the delta topset for both Experiments 1 and 2 appears to fluctuate through time. The overall trend of the observed local sedimentation rate is generally consistent with the prediction of the geometric model, since both exhibit a slow decrease with rising sea level and a subsequent approach to the sea-level rise rate ($dZ/dt = 0.0016$ and 0.0015 cm/min, respectively; Fig. 9A and B). In Experiment 3 (Fig. 9C), the aggradation rate on

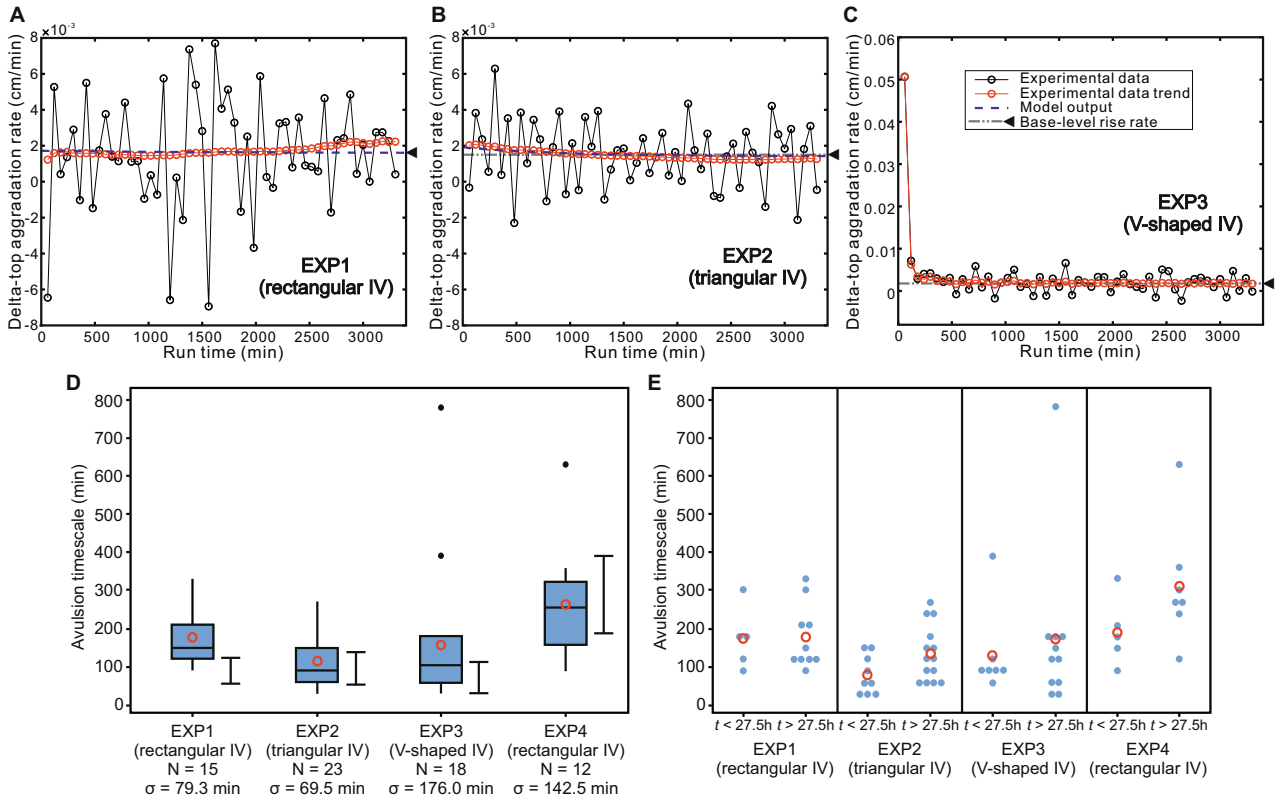

Fig. 9. Temporal variations in local aggradation rate on the delta topset and characteristic avulsion timescale of the physical experiments. (A) to (C) Temporal changes in local delta-top aggradation rate for Experiments 1 to 3, at a specific location (dashed lines shown in Fig. 8A to C), for each experiment. (D) Box plots of distributions in avulsion timescales for Experiments 1 to 4. Range plots near each box plot present predictions based on the spatially averaged mass-balance model with an imposed avulsion threshold range from 0.5 to 1.0, which corresponds to channel aggradation by 50 to 100% of the channel depth between avulsions. Other variables in the model are set to constant, representative for the current physical experiments. For each boxplot, boxes represent interquartile ranges, red open circles represent mean values, horizontal bars within the boxes represent median values, and black dots represent outliers (values that are more than 1.5 times the interquartile range). 'N' denotes the number of readings and 'σ' denotes the standard deviation. (E) Individual-value plot of observed avulsion timescales for different time intervals ($t < 27.5$ and $t > 27.5$ h) for Experiments 1 to 4. Red open circles represent mean values.

the delta topset initially decreases rapidly from a relatively high value (0.05 cm/min), until 180 min; then it fluctuates around a relatively low value, equal to the imposed sea-level rise rate ($dZ/dt = 0.0018$ cm/min). The initially high value of the aggradation rate for Experiment 3 is primarily set by the very rapid rate of river mouth progradation at the beginning of valley filling (Fig. 7A), equivalent to the progradation-dominated regime of Chadwick *et al.* (2020). As the shoreline migrates seaward, the channel necessarily responds by adjusting to maintain a transport slope, which in turn promotes vertical aggradation on the delta topset. The rates of delta-topset aggradation and imposed sea-level rise in Experiments 1 and 2 and in the later phase of Experiment 3 are comparable (Fig. 9A to C). This might be attributed to the fact that only limited shoreline migration occurs in these cases, a situation equivalent to the rise-dominated regime of Chadwick *et al.* (2020). Therefore, the deltas tend to sequester nearly all of the sediment supplied to the topset instead of transferring it to the foreset. Hence, the rate of delta topset aggradation is set by the rate of RSL rise.

Based on the overhead time-lapse images, the times for channel avulsions are identified for each experiment (Fig. 6A). The distribution of the observed avulsion timescales of the in-valley river system for each experiment (Fig. 9D) indicates that avulsions during the experiments tend to occur in a periodical manner: *average* $T_A =$

176 min for Experiment 1; *average* $T_A = 113$ min for Experiment 2; *average* $T_A = 157$ min for Experiment 3 and *average* $T_A =$ 262 min for Experiment 4. Range plots based on the prediction by the SM model assuming an imposed avulsion threshold ranging from 0.5 to 1.0 are also shown in Fig. 9D. This threshold corresponds to channel aggradation by 50 to 100% of its flow depth between avulsions (cf. Mohrig *et al.*, 2000; Ganti *et al.*, 2014). For Experiments 2 to 4, the interquartile range of the experimental results overlap with the predicted model interval significantly. The median values of experimental outputs fall within the predicted range derived from the SM model. However, for Experiment 1, only a limited overlap is observed for the experimental and predicted distribution of the avulsion timescale. Both the mean and median values are slightly higher than the highest value predicted by the SM model.

Variations in the avulsion timescale with rising sea level are explored by a comparison of the statistics of the observed characteristic avulsion timescales for different run-time intervals in the experiments ($t < 27.5$ h and $t > 27.5$ h) (Fig. 9E). Considering that the characteristic avulsion timescale of the in-valley river system scales inversely with the delta topset aggradation rate (Eq. S10), a positive relationship should be expected between the avulsion timescale and experimental run time. The mean values of avulsion timescale at later stages of the experiments ($t > 27.5$ h) are indicated to be higher than those for early stages ($t < 27.5$ h; *average* $T_A = 174$ min versus 177 min for Experiment 1; *average* $T_A = 80$ min versus 135 min for Experiment 2; *average* $T_A = 133$ min versus 172 min for Experiment 3 and *average* $T_A =$ 192 min versus 313 min for Experiment 4; Fig. 9E). This likely results from the reduced shoreline progradation rate with experimental run time (Fig. 7A), and hence reduced aggradation rates on the delta fluvial topset (Fig. 9A to C). Overall, the SM model captures the first-order variation of the characteristic avulsion timescale over the course of the experiment.

Experimental stratigraphy

To assess how avulsion events controlled the subsurface stratigraphy of fluvio-deltaic systems confined by incised valleys, strike-oriented synthetic stratigraphic panels were generated for each experiment (Fig. 10A to D; Steel *et al.*, 2022). The location of these transects, shown in Fig. 8A to C, is chosen to ensure that the stratigraphic sections run entirely through the delta-topset deposits, to avoid foreset clinoform strata. Overall, the synthetic stratigraphy (Fig. 10A to D) reveals large-scale stratigraphic architectures of distinctive channel-fill deposits in regions subject to frequent channelization, and overbank deposits in regions with limited or no channel reworking. The active channelization zones periodically shifted to lower topographic positions following avulsion, producing younger channel-fill deposits. After avulsion, newly developed channels were preferentially located either close to the two valley sidewalls or in the middle part of the valley. Specifically, in Experiment 3, for the valley with a V-shaped geometry (Fig. 10D), after an initial period of sheet flow, the flow became channelized and the active channel zones tended to shift between the two valley sidewalls for part of the experiment; only during the final phase of the experiment did the active channel zones intermittently occupy the middle portion of the valley. Note that the apparent vertical stacking of distinct channel forms shown in Fig. 10A to D is merely the result of aggradation of the same channel form through time.

To investigate how the observed surface changes of shoreline migration in the physical experiments (Fig. 7A) are recorded in the stratigraphic architecture (Fig. 10A to D), the proportion of presumed channel deposits was estimated for different shoreline migration intervals identified in the constructed synthetic stratigraphy (Fig. 10). This quantity, computed as the ratio of the sum of the areas of all channel deposits to the total area in the cross-section, describes the relative dominance of fluvial channel bodies through the stratigraphy (Fig. 10A to D; cf. Steel *et al.*, 2022). To assess whether aggradation rate and the width of the confined valley exert a control on the channel-deposit proportion, correlations between these two variables and channel-deposit proportion for different stratigraphic intervals distinguished based on their pattern of shoreline migration (Fig. 10A to D) are explored (Fig. 10E to F). An inverse relationship is identified between channel-deposit proportion versus the averaged delta-top aggradation rate for Experiment 3, whereas a positive relationship is seen for Experiment 2 (Fig. 10E). When variations are considered globally for all experiments, no negative relationship is observed between channel-deposit proportion versus the averaged delta-top aggradation rate (Fig. 10E). An inverse relationship is seen between channel-deposit proportion versus averaged valley width when data points are considered globally for all experiments (Fig. 10F).

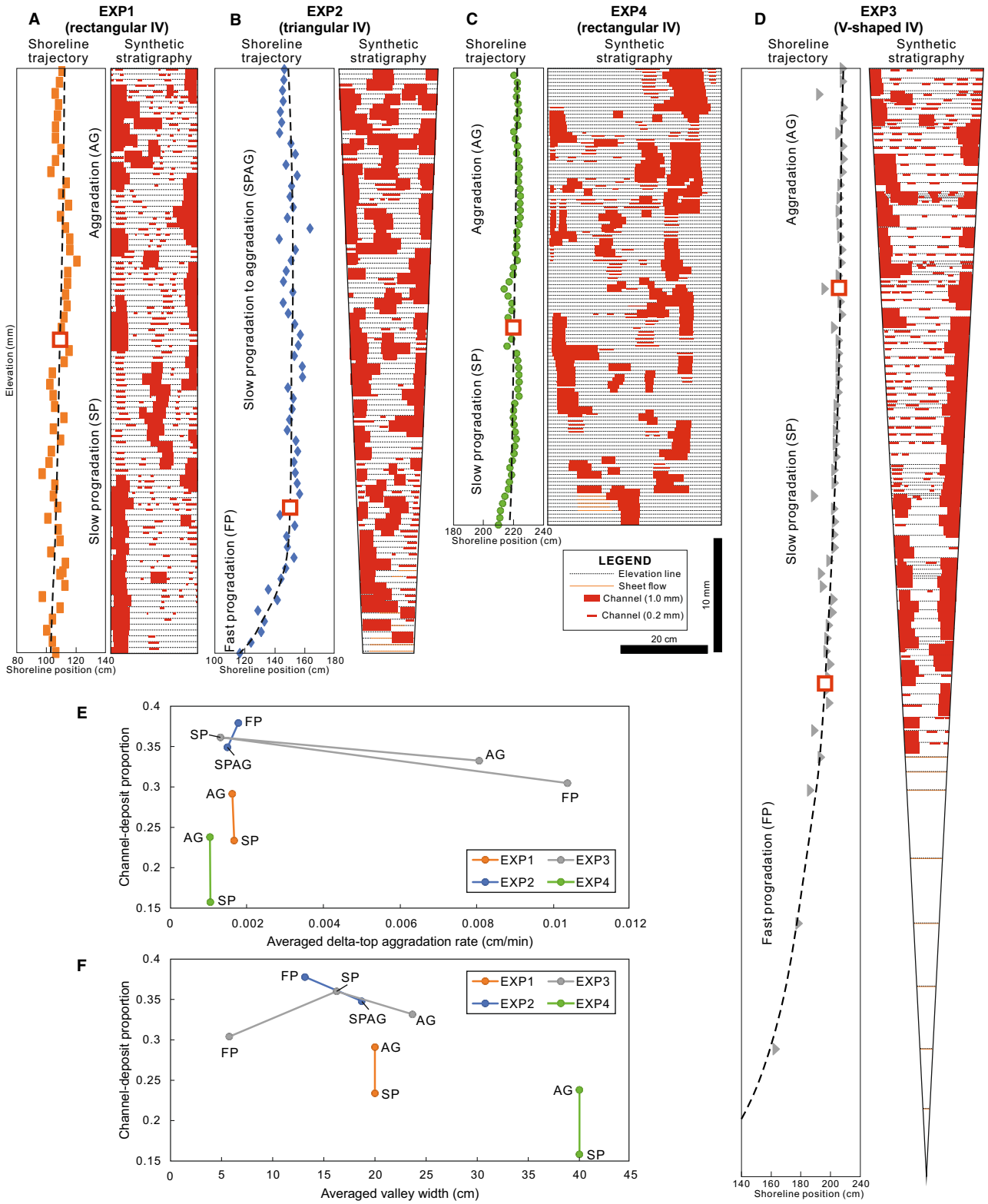

Fig. 10. (A) to (D) Strike-oriented synthetic stratigraphy generated from time-lapse overhead images (30 min) and elevation time series (1 h) for Experiments 1 to 4. Locations of sections are shown in Fig. 8A to C. Shoreline trajectories of each experiment are displayed on the left of the synthetic stratigraphies. Black dashed lines in the stratigraphic panels denote the elevation of the overbank deposits; the time interval between two successive lines is 30 min. Red boxes denote channel forms inferred to have been preserved as channel fills, orange solid lines denote inferred sheet-flow deposits and the white background denotes inferred fine-grained floodplain deposits. (E) and (F) Plots of presumed channel-deposit proportion versus (E) averaged delta-top aggradation rate, and (F) averaged confined-valley width for stratigraphic intervals distinguished based on their pattern of shoreline migration, as shown in synthetic stratigraphy (A) to (D).

DISCUSSION

Drivers of shoreline advance and retreat

Sequence stratigraphic models (e.g. Cross, 1988; Schlager, 1993) identify the rates of accommodation creation (A) and sediment supply (S) as the primary controls on shoreline advance and retreat. When sediment supply outpaces accommodation creation, delta progradation and shoreline advance occur. However, the universal validity of this principle was challenged by theoretical and experimental work from Muto and colleagues on the importance of autogenic dynamics (e.g. Muto & Steel, 1992, 2001; Muto *et al.*, 2007). Based on a 2D geometric model and 2D flume experiments, Muto and colleagues demonstrated that initial shoreline advance can evolve to retreat autogenically even under conditions of constant rates of RSL rise and sediment supply. Those authors attributed this phenomenon to the way in which sediment is partitioned within a growing delta. In essence, the A/S theory does not fully account for temporal variations in sediment partitioning between the delta topset and foreset over a growing delta. However, the autoretreat theory by Muto and colleagues was only tested in 2D and for 3D fan deltas that are free from basin topographic constraints. It neglects accommodation variations that are expected where a delta is confined by some pre-existing topography, for example, incised valleys.

Many deltas, and notably bayhead deltas, are in fact confined by incised valleys or some other form of antecedent topography, at least to a degree (e.g. Simms *et al.*, 2018). Hence, this work examines the behaviour of deltas in response to RSL rise under the interplay of the antecedent topography of an incised valley and delta geometries in 3D. Modelling outputs (Fig. 3A to J) indicate that the shoreline trajectories predicted in this work across different valley geometries generally follow the trends observed for 2D fan deltas responding to RSL rise by autoretreat. This supports the importance of the autoretreat theory (Muto, 2001; Muto *et al.*, 2007) in predicting shoreline behaviour with rising sea level.

Nevertheless, the geometric modelling and physical experiments conducted in this work, illustrate some important differences from the autoretreat theory. Based on the 2D model of Muto (2001) and Tomer *et al.* (2011), the geometric modelling and experimental setup (which includes a deltaic system with a vertical upstream boundary steeper than the foreset slope) used in this work should produce autodrowning instead of the autobreak event. However, the findings of this work indicate that, even in cases where the landward basement slope is steeper than the deltaic foreset slope (i.e. the autodrowning condition), the autobreak event can exceptionally occur if the depositional system is accommodated in an incised valley whose width increases upward (for example, valleys with a triangular or trapezoidal cross-section; Fig. 3B and C). More importantly, this work demonstrates that shoreline migration under rising sea level varies markedly depending on the geometries of both confining valleys (Figs 3, 5 and 7A) and deltas (Fig. S2). Valleys with a triangular cross-section (Fig. 3A) tend to produce shoreline trajectories with more prominent convex-seaward geometries and more rapid and seaward onsets of autoretreat and autobreak, compared to those produced in valleys with rectangular and trapezoidal cross-sectional profiles (Fig. 3B and C). Furthermore, the current model runs (Fig. S2) exhibit an increase in the seaward convexity of the shoreline trajectory as the delta-top gradient decreases. These observations highlight the critical role of the delta-topset gradient in controlling the geometric pattern of shoreline migration with rising sea level and thus provide an important update to the prediction from the numerical model based on the autoretreat theory (Muto, 2001).

In summary, this work suggests that the geometries of both the antecedent valley topography and the deltaic system growing within it

influence the onset time and rate of: (i) regression; (ii) transgression; and (iii) post-autobreak transgression under conditions of constant RSL rise and sediment supply.

Avulsion frequency during sea-level rise and implications for avulsion hazard

River avulsions expressed as abrupt shifts in river course (Mohrig *et al.*, 2000; Slingerland & Smith, 2004; Ganti *et al.*, 2014) tend to occur at characteristic locations and frequencies in large lowland deltas (Ganti *et al.*, 2014, 2016). However, how exactly the frequencies of avulsion on deltas will change in response to RSL rise (for example, caused by anthropogenic accelerated land subsidence due to fluid extraction and/or global eustatic sea-level rise), remain poorly understood. Existing observations and models (for example, the Rhine-Meuse delta, The Netherlands, Törnqvist, 1994; the Mitchell River delta, Gulf of Carpentaria, Australia, Lane *et al.*, 2017; the Mississippi and Trinity rivers, Gulf of Mexico, USA, Chatanantavet *et al.*, 2012; Moran *et al.*, 2017) diverge on whether avulsion frequency should be expected to increase or decrease with RSL rise (cf. Colombera & Mountney, 2022, 2023). In particular, limited research focuses on how the occurrence of avulsion on deltas will change with rising sea level if the deltas or bayhead deltas are constrained by incised valleys or other forms of antecedent topography. Based on theory, numerical modelling and field observations, Chadwick *et al.* (2020) indicated that avulsion frequency on large lowland deltas is determined by the balance between RSL rise and sediment supply. The same authors also found that, because most modern large deltas are experiencing reduced progradation rates compared to preindustrial conditions, projected increasing rates of RSL rise in the near future may increase delta-top aggradation rates, which might in turn accelerate channel avulsion frequency. Nevertheless, the findings observed on numerical (Fig. 4) and physical modelling (Fig. 9D and E) in this work challenge this proposition. Results indicate that changes in avulsion frequency with rising sea level vary markedly as a function of valley geometry, suggesting a major control of any antecedent topography that may confine a delta. Therefore, deltaic channels experience different avulsion frequencies depending on valley geometry, even under the same RSL rise rate (Fig. 11).

Given that most modern estuaries develop at the mouths of incised valleys, the predictions of shoreline kinematics in response to sea-level rise as a function of the antecedent topography or valley geometry in this work provide a first-order insight into future coastal changes under the global sea-level rise scenarios. The insight gained from the current study in the relationship between avulsion frequency and antecedent topography (Fig. 11) can inform the design and implementation of engineering diversions to mitigate land loss (e.g. Kim *et al.*, 2009; Paola *et al.*, 2011; Chadwick *et al.*, 2020). In particular, care must be taken in preventing and predicting catastrophic floods in future for deltas (or bayhead deltas) that are constrained by V-shaped valleys (for example, small or tributary valley systems such as the Sabine and Neches valleys along the northern Gulf of Mexico margin) and valleys with a terraced cross-section. This is because deltas confined in valleys with these geometries (Figs 3C, 3E, 4C and 4E) seem to exhibit more dramatic changes in shoreline behaviour and avulsion dynamics in response to rising sea level.

Implications for the stratigraphic record

The stratigraphy of IVFs may exhibit a basal portion characterized by amalgamated sandbodies transitioning upward to mud-dominated intervals characterized by isolated ribbon-like and sheet-like sandbodies (cf. Blum *et al.*, 2013). This reflects the expected product of temporal changes in accommodation through RSL rise: the lower amalgamated sandbodies are linked to the late lowstand and early transgressive systems tracts, whereas the overlying non-amalgamated sandbodies are linked to transgressive and early highstand systems tracts (Shanley & McCabe, 1991, 1994; Cross *et al.*, 1993; Wright & Marriott, 1993). However, the findings of this work indicate that the stratigraphic architectures of IVFs can be more complicated. In Experiments 1, 3 and 4, in the stratigraphic intervals distinguished based on the differences in shoreline migration patterns (Fig. 10A, C and D), a higher channel-deposit proportion is observed for intervals associated with aggradational (or weakly progradational for Experiment 3) stages compared to those associated with earlier phases of fast or slow progradation (Fig. 10E). This is likely due to a lower delta-top aggradation rate (Fig. 10E) at this stage arising from decreased shoreline advance rate. Higher floodplain aggradation rates are commonly thought to be linked to lower channel-body connectivity (Leeder, 1978; cf. Colombera *et al.*, 2015). During higher rates of aggradation, the thickness of preserved floodplain deposits tends to be larger than the channel scour, and therefore

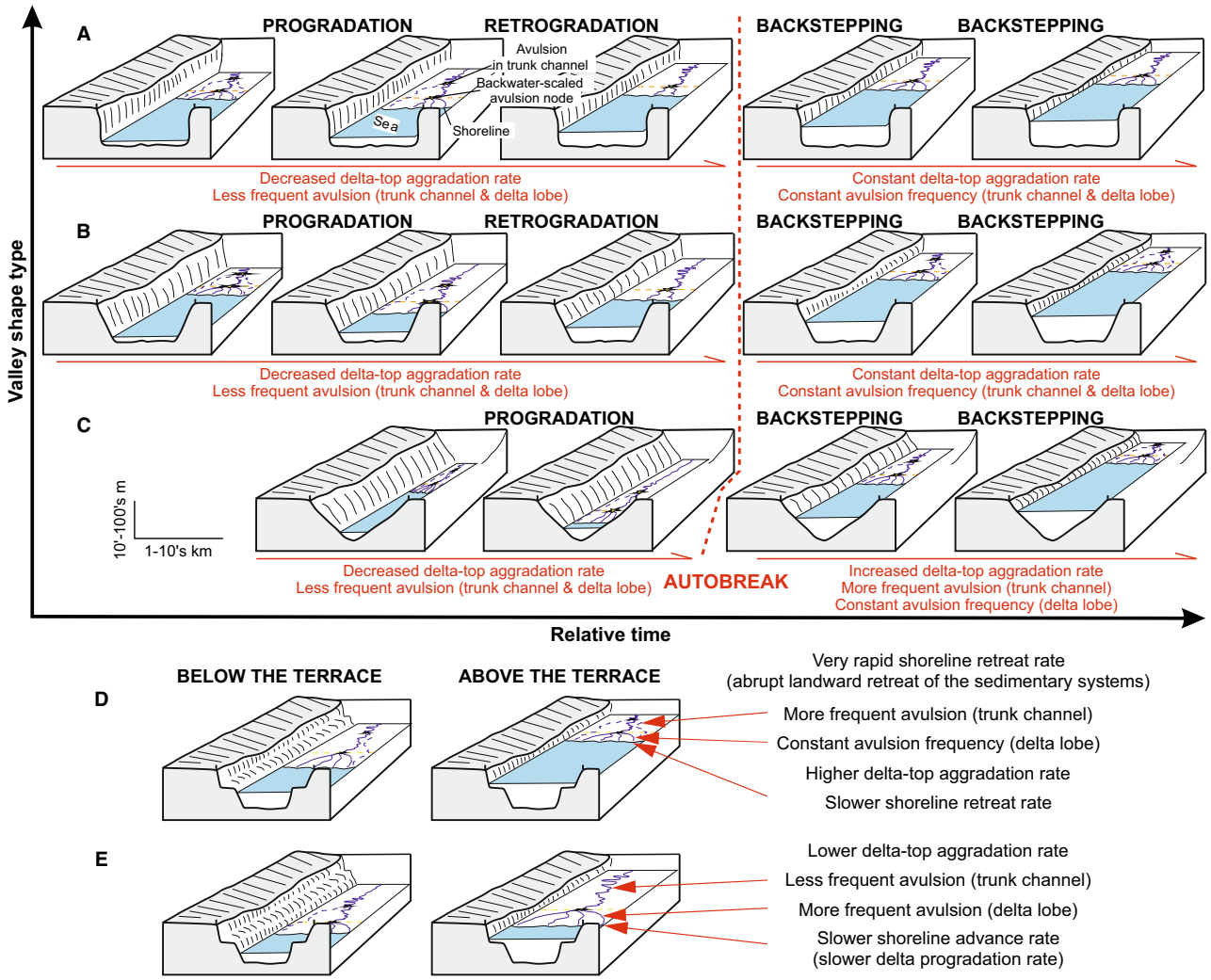

Fig. 11. Schematic diagrams (A) to (C) illustrating the temporal evolution of shoreline migration, delta-top aggradation rate and river avulsion frequency for different valley geometries under conditions of constant rates of relative sea-level (RSL) rise and sediment supply. In (D) and (E), the influence of valley terrace on a post-autobreak transgressive system (D) and a prograding delta (E) is shown, respectively.

might contribute to a lower likelihood of vertical channel-body connections and to a lower channel-deposit proportion (Steel *et al.*, 2022). Nevertheless, the anomalously high value in channel-deposit proportion (0.38) for the earlier fast progradation stage in Experiment 2 is not consistent with the high aggradation rate observed at this stage (Fig. 10E). Instead, those observations can be explained by the limited 3D accommodation available at the base of the V-shaped valley, within which channels are constrained (Fig. 10F). Moreover, an inverse relationship between valley confinement and channel-deposit proportion is seen for all experiments (Fig. 10F), highlighting the control of valley confinement on fluvial channel-body density in the stratigraphic record.

Model limitations

The present modelling approach carries uncertainty. A notable limitation lies in how different grain sizes are not considered (Fig. 3). In natural systems, a large percentage of fine-grained sediment delivered to a shoreline is deposited out of suspension from a plume that can extend far from the shoreline. This sediment can partly be deposited within the confines of incised valleys as prodelta muds. However, the current model does not consider sediment that bypasses the modelled part of the depositional profile (i.e. delta topset and foreset). Under this assumption, the model is also not applicable to deltas that exhibit a double clinoform configuration (Barrell, 1912; Nittrouer

et al., 1996; Cattaneo *et al.*, 2007). If the delta bottomset (or pro-delta mud) is considered, shoreline progradation is expected to accelerate due to a decrease in the foreset length (for example, depth at the delta front) and the retreat of the shoreline might be delayed (cf. Kim *et al.*, 2022). The magnitude of this effect depends on the amount of mud made available to the system. Additionally, the gradient of the deltaic foreset in the current geometric modelling work is set as a given value, whereas in reality it depends on grain size, basin depth and coastal reworking. Furthermore, the SM geometric model applied here evaluates the laterally averaged evolution of a depositional system inside a given valley geometry, and hence may better account for the avulsion of delta lobes as wide as the valleys in which they are contained. Finally, the effects of progressive and differential sediment compaction due to the burial of sediment beneath an overburden deltaic deposit (Törnqvist *et al.*, 2008; Chamberlain *et al.*, 2021) are ignored in the current geometric model.

Notwithstanding, the conditions considered in the current study allow exploration of the effect of valley geometry and in-valley delta geometry on shoreline migration patterns and associated avulsion dynamics. The findings of the current work remain therefore useful for better understanding of more complicated natural systems.

CONCLUSIONS

In this work, a series of geometric-based numerical models and physical experiments for a variety of prescribed incised-valley geometries, are conducted under conditions of constant rates of relative sea-level (RSL) rise and sediment supply. Overall, the current findings suggest that different aspects of antecedent topography (for example, varying valley geometries) and mass-balance interactions (varying delta geometries) can result in autogenic changes in shoreline dynamics and river avulsion frequency on deltas regardless of, or independent from, dynamic external forcing. Notably, valleys with triangular cross-sections tend to contain deltas that experience faster rates of progradation, autoretreat and post-autobreak transgression under rising sea level, and exhibit a more prominent convex-seaward shoreline trajectory, compared to valleys with rectangular and trapezoidal cross-sectional profiles. The shoreline trajectory is also related to delta topset geometry, becoming more convex-seaward under decreasing topset slopes. River avulsion frequency on delta plains subject to rising sea level varies markedly across valleys with different geometries, even under the same rate of RSL rise.

The findings in this work provide insights into future shoreline migration, and yield better understanding to predict ongoing and future coastal environmental changes in response to global sea-level rise. These are essential for protecting vulnerable populations, infrastructures and industries located in large coastal cities. Moreover, the current findings provide a quantitative framework for spatiotemporal variability in avulsion dynamics (i.e. avulsion frequency and avulsion location; Figs 3 and 4) in valley-confined deltas. This in turn has implications for the mitigation of catastrophic flood hazards associated with avulsion events (i.e. the avulsion hazards need to shift upstream or downstream as the avulsion node would migrate in tandem with the shoreline along the dip direction). This also provides insight into the design of effective river diversions that mimic the natural tendency of rivers to undertake more or less frequent avulsions on engineered and built-upon land, which can mitigate land loss against the accelerating global sea-level rise (e.g. Kim *et al.*, 2009; Paola *et al.*, 2011; Chadwick *et al.*, 2020). Furthermore, observations of autogenic shoreline kinematics under rising sea level, together with those on associated changes in autogenic behaviours such as delta-lobe switching (avulsion) (Fig. 10A to D) and backwater dynamics during sea-level rise (Fig. 4; Moran *et al.*, 2017), reveal the potential importance of these mechanisms as controls on the stratigraphic variations in the ancient rock record. The importance of internal dynamics as a driver of stratigraphic changes in the absence of dynamic external forcing has recently received considerable attention (for example, compensational stacking, Mutti & Sonnino, 1981; Mohrig *et al.*, 2000; fluvial terraces generated by auto-incision, Muto & Steel, 2004; auto-reorganization of fluvial systems in hanging-wall basins, Kim & Paola, 2007). The findings in this work expand the current understanding of internal feedbacks in sediment-routing systems and their resultant stratigraphic record, which in turn can provide important insight for discerning stratigraphic products of autogenic processes from the stratigraphic signals of climatic, tectonic and sea-level changes (Hajek *et al.*, 2010; Burgess *et al.*, 2019; Toby *et al.*, 2019; Straub *et al.*, 2020).

ACKNOWLEDGEMENTS

Members of Morphodynamics–Quantitative Stratigraphy lab. at Yonsei University, South Korea are thanked for assistance in the initial set up of the physical experiments. Dave M. Hodgson from University of Leeds, UK, is thanked for providing critical and constructive comments on an earlier draft of this work. RW thanks the International Association of Sedimentologists for provision of a Post-Doctoral Research Grant that enabled physical experiment conduction for part of this study. This research is also partly supported by the Basic Science Research Program through the National Research Foundation of Korea (NRF), which is funded by the Ministry of Education (NRF-2017R1A6A1A07015374) and Korea Institute of Energy Technology Evaluation and Planning (KETEP) grant funded by the Korea government (MOTIE-20212010200010) to WK. LC and NPM thank the sponsors and partners of FRG-ERG-SMRG for financial support: AkerBP, Areva (now Orano), BHPBilliton, Cairn India (Vedanta), ConocoPhillips, Chevron, Debmarine, Engie, Equinor, Murphy Oil, Nexen-CNOOC, Occidental, Petrotechnical Data Systems, Saudi Aramco, Shell, Tullow Oil, Woodside and YPF. Associate Editor Kyle Straub, Prof. Alex Simms and an anonymous reviewer are thanked for their constructive comments, which have substantially improved the article.

NOMENCLATURE

Symbol	Definition	Dimensions (L = length, M = mass, T = time, 1 = dimensionless)
A	Rate of accommodation creation	$L^3\,T^{-1}$
A_V	Valley strike cross-sectional area	L^2
b	Elevation of the basement	L
B	Delta lobe width	L
dt	Time step	T
dS/dt	Shoreline migration rate	$L\,T^{-1}$
dR/dt	Volumetric accommodation available for sedimentation within the valley at each time step, i.e. three-dimensional accommodation creation rate	$L^3\,T^{-1}$
dZ/dt	Rate of relative base-level rise	$L\,T^{-1}$
D	Delta lobe progradation distance	L
f_A	Avulsion frequency	T^{-1}
Fr	Froude number	1
g	Acceleration due to gravity	$L\,T^{-2}$
h_1	Elevation of the terrace or height between the valley end and elevation of the valley base at the slope break	L
h_2	Height between elevation of the valley base at the slope break and the slope break	L
h_3	Height between the valley head and the slope break	L
h_n	Normal flow depth	L
H	Valley height	L
H_a	Aggradation thickness necessary for avulsion	L
H^*	Avulsion threshold	1
H_b	Offshore basin depth	L
H_c	Bankfull channel depth	L
H_e	Total elevation extent of the valley thalweg	L
L_{auto}	Autostratigraphic length scale	L
L_A	Lobe length (or avulsion length)	L

Symbol	Definition	Dimensions (L = length, M = mass, T = time, 1 = dimensionless)
L_b	Backwater length	L
L_v	Horizontal valley length	L
n	Number of avulsions before a given lobe is occupied	1
N	Number of delta lobes	1
q_s	Rate of sediment supply per unit width	$L^2 T^{-1}$
Q_s	Volumetric sediment supply	$L^3 T^{-1}$
Q_w	Volumetric water discharge	$L^3 T^{-1}$
s_s	Position of shoreline (delta topset–foreset break)	L
s_{auto}	Shoreline position at time of autobreak	L
s_M	Shoreline position at the maximum seaward advance point	L
s_{sb}	Position of delta toe (foreset–subaqueous basement break)	L
S_c	Channel bed slope	1
S_f	Delta foreset slope	1
S_t	Delta topset slope	1
t	Time	T
t_{auto}	Time to autobreak	T
T_{auto}	Autostratigraphic timescale	T
T_A	Avulsion timescale	T
Δt	Step length in time t	T
U	Depth-averaged flow velocity	$L T^{-1}$
V	Total volume of sediment deposited in the valley over time t or volume available for sediment deposition in the valley	L^3
V_a	Aggradation rate	$L T^{-1}$
W	Valley width	L
W_1	Valley width at the base for valley with a terraced strike cross-section	L
W_2	Valley width at the terrace for valley with a terraced strike cross-section	L
W_Z	Instantaneous valley width at the elevation of sea level at a given time	L
x	Downstream distance	L
z	Cumulative magnitude of RSL rise during an interavulsion period	L
Z	Elevation of the base level	L
Z_{auto}	Elevation of the base level at time of autobreak	L
Z_i	Elevation of the initial base level	L
α	Slope of valley thalweg	1
β	Slope of the landward interfluve	1
η_{sauto}	Elevation of the shoreline at time of autobreak	L
η_0	Elevation of the bedrock–alluvial transition	L
η_s	Bed elevation at the shoreline	L
ϕ	Slope of the seaward interfluve	1
λ_p	Porosity of sediment	1
θ	Valley sidewall slope	1

DATA AVAILABILITY STATEMENT

The data that support the findings of this study are available from the corresponding authors upon reasonable request.

REFERENCES

Anderson, J.B., **Rodriguez, A.**, **Abdulah, K.C.**, **Fillon, R.H.**, **Banfield, L.A.**, **McKeown, H.A.** and **Wellner, J.S.** (2004) Late Quaternary stratigraphic evolution of the northern Gulf of Mexico margin: a synthesis. In: *Late Quaternary Stratigraphic Evolution of the Northern Gulf of Mexico Margin: A Synthesis* (Eds Anderson, J.B. and Fillon, R.H.), *SEPM Spec. Publ.*, **79,** 1–23. SEPM (Society for Sedimentary Geology), Tulsa, Oklahoma, USA.

Barrell, J. (1912) Criteria for the recognition of ancient delta deposits. *Geol. Soc. Am. Bull.*, **23**, 377–446.

Baumanis, C. and **Kim, W.** (2018) Reverse migration of lithofacies boundaries and shoreline in response to sea-level rise. *Basin Res.*, **30**, 89–100.

Blum, M.D. and **Törnqvist, T.E.** (2000) Fluvial responses to climate and sea-level change: a review and look forward. *Sedimentology*, **47**, 2–48.

Blum, M.D., **Martin, J.**, **Milliken, K.** and **Garvin, M.** (2013) Paleovalley systems: insights from Quaternary analogs and experiments. *Earth-Sci. Rev.*, **116**, 128–169.

Bowen, D.W. and **Weimer, P.** (2003) Regional sequence stratigraphic setting and reservoir geology of Morrow incised-valley sandstones (lower Pennsylvanian), eastern Colorado and western Kansas. *AAPG Bull.*, **87**, 781–815.

Burgess, P.M., **Masiero, I.**, **Toby, S.C.** and **Duller, R.A.** (2019) A big fan of signals? Exploring autogenic and allogenic process and product in a numerical stratigraphic forward model of submarine-fan development. *J. Sediment. Res.*, **89**, 1–12.

Cattaneo, A., **Trincardi, F.**, **Asioli, A.** and **Correggiari, A.** (2007) The Western Adriatic shelf clinoform: energy-limited bottomset. *Cont. Shelf Res.*, **27**, 506–525.

Catuneanu, O. (2006) *Principles of Sequence Stratigraphy*. Elsevier, Amsterdam, Netherland.

Chadwick, A.J. and **Lamb, M.P.** (2021) Climate-change controls on river delta avulsion location and frequency. *J. Geophys. Res. Earth Surf.*, **126**, e2020JF005950.

Chadwick, A.J., **Lamb, M.P.** and **Ganti, V.** (2020) Accelerated river avulsion frequency on lowland deltas due to sea-level rise. *Proc. Natl Acad. Sci. USA*, **117**, 17584–17590.

Chamberlain, E.L., **Shen, Z.**, **Kim, W.**, **McKinley, S.**, **Anderson, S.** and **Tornqvist, T.E.** (2021) Does load-induced shallow subsidence inhibit delta growth? *J. Geophys. Res. Earth Surf.*, **126**, e2021JF006153.

Chatanantavet, P., **Lamb, M.P.** and **Nittrouer, J.A.** (2012) Backwater controls of avulsion location on deltas. *Geophys. Res. Lett.*, **39**, L01402.

Colombera, L. and **Mountney, N.P.** (2022) Scale dependency in quantifications of the avulsion frequency of coastal rivers. *Earth-Sci. Rev.*, **230**, 104043.

Colombera, L. and **Mountney, N.P.** (2023) Downstream controls on coastal-plain river avulsions: a global study. *J. Geophys. Res. Earth Surf.*, **128**, e2022JF006772.

Colombera, L., **Mountney, N.P.** and **McCaffrey, W.D.** (2015) A meta-study of relationships between fluvial channel-body stacking pattern and aggradation rate: implications for sequence stratigraphy. *Geology*, **43**, 283–286.

Cross, T.A. (1988) Controls on coal distribution in transgressive-regressive cycles, Upper Cretaceous, Western Interior, USA. In: *Sea-Level Changes: An Integrated Approach* (Eds Wilgus, C.K., Hastings, B.S., Kendall, C.G.C., Posamentier, H.W., Ross, C.A. and van Wagoner, J.C.), *SEPM Spec. Publ.*, **42**, 125–154. SEPM (Society for Sedimentary Geology), Tulsa, Oklahoma, USA.

Cross, T.A., **Baker, M.R.**, **Chapin, M.A.**, **Clark, M.S.**, **Gardner, M.H.**, **Hanson, M.S.**, **Lessenger, M.A.**, **Little, L.D.**, **McDonough, K.J.**, **Sonnenfield, M.D.**, **Valasek, D.W.**, **Williams, M.R.** and **Witter, D.N.** (1993) Applications of high-resolution sequence stratigraphy to reservoir analysis. In: *Subsurface Reservoir Characterization from Outcrop Observations* (Eds Eschard, R. and Doligez, B.), *Proceedings 7th IFP Exploration and Production Conference*, pp. 11–33. Editions Technip, Paris, France.

Dalrymple, R.W. and **Zaitlin, B.A.** (1994) High-resolution sequence stratigraphy of a complex, incised valley succession, the Cobequid Bay–Salmon River estuary, Bay of Fundy, Canada. *Sedimentology*, **41**, 1069–1091.

Dalrymple, R.W., **Zaitlin, B.A.** and **Boyd, R.** (1992) Estuarine facies models: conceptual basis and stratigraphic implications. *J. Sed. Petrol.*, **62**, 1130–1146.

Ganti, V., **Chu, Z.**, **Lamb, M.P.**, **Nittrouer, J.A.** and **Parker, G.** (2014) Testing morphodynamic controls on the location and frequency of river avulsions on fans versus deltas: Huanghe (Yellow River), China. *Geophys. Res. Lett.*, **41**, 7882–7890.

Ganti, V., **Chadwick, A.J.**, **Hassenruck-Gudipati, H.J.**, **Fuller, B.M.** and **Lamb, M.P.** (2016) Experimental river delta size set by multiple floods and backwater hydrodynamics. *Sci. Adv.*, **2**, e1501768.

Graf, W.H. (1998) *Fluvial Hydraulics: Flow and Transport Processes in Channels of Simple Geometry*. John Wiley & Sons, Chichester, UK, 681 pp.

Guerit, L., **Foreman, B.Z.**, **Chen, C.**, **Paola, C.** and **Castelltort, S.** (2020) Autogenic delta progradation during sea-level rise within incised valleys. *Geology*, **49**, 273–277.

Hajek, E.A. and **Straub, K.M.** (2017) Autogenic sedimentation in clastic stratigraphy. *Annu. Rev. Earth Planet. Sci.*, **45**, 681–709.

Hajek, E.A., **Heller, P.L.** and **Sheets, B.A.** (2010) Significance of channel-belt clustering in alluvial basins. *Geology*, **38**, 535–538.

Hampson, G.J., **Davies, S.J.**, **Elliott, T.**, **Flint, S.S.** and **Stollhofen, H.** (1999) Incised valley fillsandstone bodies in Upper Carboniferous fluvio–deltaic strata: recognition andreservoir characterization of Southern North Sea analogues. In: *Petroleum Geology ofNorthwest Europe: Proceedings of the 5th Conference* (Eds Fleet, A.J. and Boldy, S.A.R.), **5**, 771–788. The Geological Society, London, London.

Helland-Hansen, W. and **Martinsen, O.J.** (1996) Shoreline trajectories and sequences; description of variable depositional-dip scenarios. *J. Sediment. Res.*, **66**, 670–688.

Holbrook, J.M., **Scott, R.W.** and **Oboh-Ikuenobe, F.E.** (2006) Base-level buffers and buttresses: a model for upstream verses downstream control on preservation of fluvial geometry and architecture within sequences. *J. Sed. Res.*, **76**, 162–174.

Jerolmack, D.J. and **Mohrig, D.** (2007) Conditions for branching in depositional rivers. *Geology*, **35**, 463–466.

Kim, W. and **Paola, C.** (2007) Long-period cyclic sedimentation with constant tectonic forcing in an experimental relay ramp. *Geology*, **35**, 331–334.

Kim, W., **Paola, C.**, **Voller, V.R.** and **Swenson, J.B.** (2006) Experimental measurement of the relative importance of controls on shoreline migration. *J. Sediment. Res.*, **76**, 270–283.

Kim, W., **Mohrig, D.**, **Twilley, R.R.**, **Paola, C.** and **Parker, G.** (2009) Is it feasible to build new land in the Mississippi River delta? *Eos*, **90**, 373–374.

Kim, M., **Kim, W.** and **Nahm, W.H.** (2022) The effect of bottomset on fluviodeltaic land-building process: numerical modelling and physical experiment. *Basin Res.*, **34**, 1763–1780.

Lane, T.I., **Nanson, R.A.**, **Vakarelov, B.K.**, **Ainsworth, R.B.** and **Dashtgard, S.E.** (2017) Evolution and architectural styles of a forced-regressive Holocene delta and megafan, Mitchell River, Gulf of Carpentaria, Australia. *Geol. Soc. Lond. Spec. Publ.*, **444**, 305–334.

Leeder, M.R. (1978) A quantitative stratigraphic model for alluvium, with special reference to channel deposit density and interconnectedness. In: *Fluvial Sedimentology* (Ed Miall, A.D.), *Memoirs Canadian Society of Petroleum Geology*, **5**, 587–596. Canadian Society of Petroleum Geologists, Calgary, Canada.

Leopold, L.B., **Wolman, M.G.** and **Miller, J.P.** (1964) *Fluvial Processes in Geomorphology*. Dover Publications, New York, US. 522 pp.

Martin, J., **Sheets, B.**, **Paola, C.** and **Hoyal, D.** (2009) Influence of steady base-level rise on channel mobility, shoreline migration, and scaling properties of a cohesive experimental delta. *J. Geophys. Res.*, **114**, F03017.

Matthes, G.H. (1956) River surveys in unmapped territory. *Trans. Am. Soc. Civ. Eng.*, **121**, 739–752.

Milton, N.J. and **Bertram, G.T.** (1995) Topset play types and their controls. In: *Sequence Stratigraphy of Foreland Basin Deposits, Outcrop and Subsurface Examples from the Cretaceous of North America* (Eds van Wagoner, J.C. and Bertram, G.T.), *American Association of Petroleum Geologists, Memoir*, **64**, 1–9. AAPG (The American Association of Petroleum Geologists), Tulsa, Oklahoma, USA.

Mohrig, D., **Heller, P.L.**, **Paola, C.** and **Lyons, W.J.** (2000) Interpreting avulsion process from ancient alluvial sequences: Guadalope-Matarranya system (northern Spain) and Wasatch Formation (western Colorado). *Geol. Soc. Am. Bull.*, **112**, 1787–1803.

Moran, K.E., **Nittrouer, J.A.**, **Perillo, M.M.**, **Lorenzo-Trueba, J.** and **Anderson, J.B.** (2017) Morphodynamic modeling of fluvial channel fill and avulsion time scales during early Holocene transgression, as substantiated by the incised valley stratigraphy of the Trinity River, Texas. *J. Geophys. Res. Earth Surf.*, **122**, 215–234.

Muto, T. (2001) Shoreline autoretreat substantiated in flume experiments. *J. Sediment. Res.*, **71**, 246–254.

Muto, T. and **Steel, R.J.** (1992) Retreat of the front in a prograding delta. *Geology*, **20**, 967–970.

Muto, T. and **Steel, R.J.** (1997) Principles of regression and transgression; the nature of the interplay between accommodation and sediment supply. *J. Sediment. Res.*, **67**, 994–1000.

Muto, T. and **Steel, R.J.** (2001) Autostepping during the transgressive growth of deltas: results from flume experiments. *Geology*, **29**, 771–774.

Muto, T. and **Steel, R.J.** (2004) Autogenic response of fluvial deltas to steady sea-level fall: implications from flume-tank experiments. *Geology*, **32**, 401–404.

Muto, T., **Steel, R.J.** and **Swenson, J.B.** (2007) Autostratigraphy: a framework norm for genetic stratigraphy. *J. Sediment. Res.*, **77**, 2–12.

Mutti, E. and **Sonnino, M.** (1981) Compensational Cycles: A Diagnostic Feature of Turbidite Sandstone Lobes. Paper presented at the *International Association of Sedimentologists, Second European Regional Meeting*, pp. 120–123.

Nittrouer, C.A., **Kuehl, S.A.**, **Figueiredo, A.G.**, **Allison, M.A.**, **Sommerfield, C.K.**, **Rine, J.M.**, **Faria, L.E.C.** and **Silveira, O.M.** (1996) The geological record preserved by Amazon shelf sedimentation. *Cont. Shelf Res.*, **16**, 817–841.

Paola, C., **Twilley, R.R.**, **Edmonds, D.A.**, **Kim, W.**, **Mohrig, D.**, **Parker, G.**, **Viparelli, E.** and **Voller, V.R.** (2011) Natural processes in delta restoration: Application to the Mississippi Delta. *Annu. Rev. Mar. Sci.*, **3**, 67–91.

Parker, G., **Muto, T.**, **Akamatsu, Y.**, **Dietrich, W.E.** and **Lauer, J.W.** (2008a) Unravelling the conundrum of river response to rising sea-level from laboratory to field. Part I: laboratory experiments. *Sedimentology*, **55**, 1643–1655.

Parker, G., **Muto, T.**, **Akamatsu, Y.**, **Dietrich, W.E.** and **Lauer, J.W.** (2008b) Unravelling the conundrum of river response to rising sea-level from laboratory to field. Part II: the Fly–Strickland River system, Papua New Guinea. *Sedimentology*, **55**, 1657–1686.

Posamentier, H.W. and **Allen, G.P.** (1999) *Siliciclastic Sequence Stratigraphy: Concepts and Applications*. SEPM (Society for Sedimentary Geology), Tulsa, Oklahoma, 210 pp.

Posamentier, H.W. and **Vail, P.R.** (1988) Eustatic control on clastic deposition II—sequence and system tract models. In: *Sea-Level Changes: An Integrated Approach* (Eds Wilgus, C.K., Hastings, B.S., Kendall, C.G.C., Posamentier, H.W., Ross, C.A. and van Wagoner, J.C.), *SEPM Spec. Publ.*, **42**, 125–154. SEPM (Society for Sedimentary Geology), Tulsa, Oklahoma, USA.

Posamentier, H.W., **Jervey, M.T.** and **Vail, P.R.** (1988) Eustatic controls on clastic deposition I—conceptual framework. In: *Sea-Level Changes: An Integrated Approach* (Eds Wilgus, C.K., Hastings, B.S., Kendall, C.G.C., Posamentier, H.W., Ross, C.A. and van Wagoner, J.C.), *SEPM Spec. Publ.*, **42**, 125–154. SEPM (Society for Sedimentary Geology), Tulsa, Oklahoma, USA.

Rodriguez, A.B., **Anderson, J.B.** and **Simms, A.R.** (2005) Terrace inundation as an autocyclic mechanism for parasequence formation: Galveston Estuary, Texas, USA. *J. Sed. Res.*, **75**, 608–620.

Rodriguez, A.B., **Greene, D.L.**, **Anderson, J.B.** and **Simms, A.R.** (2008) Response of Mobile Bay and eastern Mississippi Sound, Alabama, to changes in sediment accommodation and accumulation. *Geol. Soc. Am. Spec.*, **443**, 13–29.

Sahoo, H. and **Gani, M.R.** (2016) Autogenic modulation of fluvial channel fills in allogenically formed incised valleys: cretaceous Blackhawk Formation, USA. In: *Autogenic Dynamics in Sedimentary Systems* (Eds Budd, D.A., Hajek, E.A. and Purkis, S.J.), *SEPM Spec. Publ.*, **106**, 163–175. SEPM (Society for Sedimentary Geology), Tulsa, Oklahoma, USA.

Salem, A.M., **Ketzer, J.M.**, **Morad, S.**, **Rizk, R.R.** and **Al-Aasm, I.S.** (2005) Diagenesis and reservoir-quality evolution of incised-valley sandstones: evidence from the Abu Madi gas reservoirs (Upper Miocene), the Nile Delta basin, Egypt. *J. Sediment. Res.*, **75**, 572–584.

Schlager, W. (1993) Accommodation and supply-A dual control on stratigraphic sequences. *Sediment. Geol.*, **86**, 111–136.

Shanley, K.W. and **McCabe, P.J.** (1991) Predicting facies architecture through sequence stratigraphy—an example

from the Kaiparowits Plateau, Utah. *Geology*, **19**, 742–745.

Shanley, K.W. and **McCabe, P.J.** (1994) Perspectives on the sequence stratigraphy of continental strata: report of a working group at the 1991 NUNA conference of high resolution sequence stratigraphy. *AAPG Bull.*, **78**, 544–568.

Sheets, B.A., **Paola, C.** and **Kelberer, J.M.** (2007) Creation and preservation of channel-form sand bodies in an experimental alluvial system. In: *Sedimentary Processes, Environments and Basins* (Eds Nichols, G.J., Williams, E. and Paola, C.), *IAS Spec. Publ.*, **38**, 555–567. Blackwell, Oxford, UK.

Simms, A.R. and **Rodriguez, A.B.** (2014) Where do coastlines stabilize following rapid retreat? *Geophys. Res. Lett.*, **41**, 1698–1703.

Simms, A.R. and **Rodriguez, A.B.** (2015) The influence of valley morphology on the rate of bayhead delta progradation. *J. Sed. Res.*, **85**, 38–44.

Simms, A.R., **Rodriguez, A.B.** and **Anderson, J.B.** (2018) Bayhead deltas and shorelines: insights from modern and ancient examples. *Sediment. Geol.*, **374**, 17–35.

Slingerland, R. and **Smith, N.D.** (2004) River avulsions and their deposits. *Annu. Rev. Earth Planet. Sci.*, **32**, 257–285.

Steel, E., **Paola, C.**, **Chadwick, A.J.**, **Hariharan, J.**, **Passalacqua, P.**, **Xu, Z.**, **Michael, H.A.**, **Brommecker, H.** and **Hajek, E.A.** (2022) Reconstructing subsurface sandbody connectivity from temporal evolution of surface networks. *Basin Res.*, **34**, 1486–1506.

Stephen, K.D. and **Dalrymple, M.** (2002) Reservoir simulations developed from an outcrop of incised valley fill strata. *AAPG Bull.*, **86**, 797–822.

Straub, K.M., **Ganti, V.**, **Paola, C.** and **Foufoula-Georgiou, E.** (2012) Prevalence of exponential bed thickness distributions in the stratigraphic record: Experiments and theory. *J. Geophys. Res.*, **117**, F02003.

Straub, K.M., **Duller, R.A.**, **Foreman, B.Z.** and **Hajek, E.A.** (2020) Buffered, incomplete, and shredded: The challenges of reading an imperfect stratigraphic record. *J. Geophys. Res. Earth Surf.*, **125**, e2019JF005079.

Summerfield, M.A. (1985) Plate tectonics and landscape development on the African continent. In: *Tectonic Geomorphology* (Eds Morisawa, M. and Hack, J.), pp. 27–51. Allen and Unwin, Boston.

Talling, P.J. (1998) How and where do incised valleys form if sea level remains above the shelf edge? *Geology*, **26**, 87–90.

Toby, S.C., **Duller, R.A.**, **De Angelis, S.** and **Straub, K.M.** (2019) A stratigraphic framework for the preservation and shredding of environmental signals. *Geophys. Res. Lett.*, **46**, 5837–5845.

Tomer, A., **Muto, T.** and **Kim, W.** (2011) Autogenic hiatus in fluviodeltaic successions: geometrical modeling and physical experiments. *J. Sediment. Res.*, **81**, 207–217.

Törnqvist, T.E. (1994) Middle and late Holocene avulsion history of the river Rhine (Rhine-Meuse delta, Netherlands). *Geology*, **22**, 711–714.

Törnqvist, T.E., **Wallace, D.J.**, **Storms, J.E.**, **Wallinga, J.**, **Van Dam, R.L.**, **Blaauw, M.**, **Derksen, M.S.**, **Klerks, C.J.**, **Meijneken, C.** and **Snijders, E.** (2008) Mississippi Delta subsidence primarily caused by compaction of Holocene strata. *Nat. Geosci.*, **1**, 173–176.

Van Wagoner, J.C., **Mitchum, R.M.**, **Campion, K.M.** and **Rahmanian, V.D.** (1990) Siliciclastic sequence stratigraphy in well logs, core, and outcrops: concepts for high resolution correlation of time and facies. *Am. Assoc. Petrol. Geol. Meth. Explor. Ser.*, **7**, 55.

Wang, R., **Colombera, L.** and **Mountney, N.P.** (2019) Geologic controls on the geometry of incised-valley fills: insights from a global dataset of late-quaternary examples. *Sedimentology*, **66**, 2134–2168.

Wang, R., **Colombera, L.** and **Mountney, N.P.** (2020) Database-driven quantitative analysis of the stratigraphic architecture of incised-valley fills. *Earth-Sci. Rev.*, **102**, 1–25.

Wright, V.P. and **Marriott, S.B.** (1993) The sequence stratigraphy of fluvial depositional systems: the role of floodplain sediment storage. *Sed. Geol.*, **86**, 203–210.

Zaitlin, B.A., **Dalrymple, R.W.** and **Boyd, R.** (1994) The stratigraphic organization of incisedvalley systems associated with relative sea-level change. In: *Incised-Valley Systems: Origin and Sedimentary Sequences* (Eds Dalrymple, R.W., Boyd, R. and Zaitlin, B.A.), *SEPM Spec. Publ.*, **51**, 45–60. SEPM (Society for Sedimentary Geology), Tulsa, Oklahoma, USA.

Manuscript received 15 February 2023; revision accepted 8 January 2024

Supporting Information

Additional information may be found in the online version of this article:

Data S1 Supporting Information 1: Derivation of the analytical models to simulate the shoreline migration patterns for simple valley geometries.

Supporting Information 2: Derivation of the analytical models for the estimation of the characteristic avulsion timescale.

Supporting Information 3: Derivation of relevant parameters considered in the geometric model.

Supporting Information 4: Physical experiments.

Supporting Information 5: Workflow for the construction of synthetic stratigraphy.

Supporting Information 6: Modelled outputs for the dynamic of delta topset aggradation rate with rising sea level.

Supporting Information 7: Sensitivity analysis of the seaward interfluve slope, ϕ, on the model outputs.

Supporting Information 8: Detailed comparison between the experimental shoreline trajectory observed in the stacked digital elevation models and that shown in the geometric model outputs.

Figure S1. (**A**) Model conceptualization for the numerical calculation of the instantaneous valley width, W_Z, at the elevation of base level, Z, in response to linear sea-level rise at a given time, t. Shaded regions indicate the sediments deposited in the valley at the elevation of base level, Z. (**B**) Model conceptualization for the numerical calculation of

cross-section-averaged valley width, W_N. Valley width, W, valley height, H, and valley strike cross-sectional area, A_V, are indicated.

Figure S2. Non-dimensional shoreline trajectories for different valley geometries (simple valley geometry) and different deltaic geometries (i.e. variations of the inclination of delta topset slope).

Movie S1. Movie S1. Experimental evolution of delta confined in a valley with rectangular strike cross-sectional profile and constant morphology in the dip direction (Experiment 1).

Movie S2. Experimental evolution of delta confined in a valley with triangular strike cross-sectional profile and constant morphology in the dip direction (Experiment 2).

Movie S3. Experimental evolution of delta confined in a valley with V-shaped geometry (Experiment 3).

Movie S4. Experimental evolution of delta confined in a valley with rectangular strike cross-sectional profile and constant morphology in the dip direction (Experiment 4).